Anharmonic properties from a generalized third-order *ab initio* approach: Theory and applications to graphite and graphene

Lorenzo Paulatto,* Francesco Mauri, and Michele Lazzeri
IMPMC, Université Pierre et Marie Curie, CNRS, 4 place Jussieu, F-75005 Paris, France
(Received 9 April 2013; published 7 June 2013)

We have implemented a generic method, based on the $2n + 1$ theorem within density functional perturbation theory, to calculate the anharmonic scattering coefficients among three phonons with arbitrary wave vectors. The method is used to study the phonon broadening in graphite and graphene mono- and bilayers. The broadening of the high-energy optical branches is highly nonuniform and presents a series of sudden steps and spikes. At finite temperature, the two linearly dispersive acoustic branches TA and LA of graphene have nonzero broadening for small wave vectors. The broadening in graphite and bilayer graphene is, overall, very similar to the graphene one, the most remarkable feature being the broadening of the quasiacoustical Z-polarized branch. Finally, we study the intrinsic anharmonic contribution to the thermal conductivity of the three systems, within the single mode relaxation time approximation. We find the conductance to be in good agreement with experiments in the out-of-plane direction but underestimate by a factor 2 in-plane.

DOI: 10.1103/PhysRevB.87.214303 PACS number(s): 63.20.kg, 63.20.dk, 63.22.Rc, 65.80.Ck

I. INTRODUCTION

Thermal transport is currently attracting much attention; the main applications of interest are materials for thermoelectric energy conversion[1] and materials used for thermal dissipation in microelectronics.[2] While, in the first case, the goal is to engineer the smallest possible thermal conduction, in the second case, a good thermal conduction is required. In general, our understanding of thermal properties is heavily based on theoretical modeling, and the use of precise and reliable approaches, such as the *ab initio* computational methods, is highly desirable.

The presence of a temperature gradient in a solid induces a heat flux. The heat carriers can be lattice vibrations (phonons) or electronic excitations. In general, lattice conduction is the dominant mechanism in the presence of an electronic gap (semiconductors and insulators) or when the gap is zero but the density of electronic states at the Fermi level is small (semimetals). Lattice thermal resistance is then dictated by phonon scattering, which can be induced by extrinsic mechanisms (isotopic disorder, structural defects, finite-size of the crystals, etc.) or by intrinsic ones (anharmonic phonon-phonon scattering). Determining the intrinsic anharmonic scattering is in itself a very complex task; it has been attempted *ab initio*, within density functional theory (DFT), using finite difference derivation[3,4] or molecular dynamics techniques,[5] or from linear response theory.[6–9]

In a crystal, the intrinsic lattice thermal conduction can be obtained by knowing harmonic phonon energies and anharmonic phonon-phonon scattering coefficients. Harmonic phonon energies are determined by the second-order derivative of the system total energy, with respect to atomic displacements. This second derivative can be efficiently calculated *ab initio* by using density functional perturbation theory (DFPT),[10] which allows the determination of the phonon dynamical matrix for an arbitrary $\mathbf{q}$ wave vector in the Brillouin zone. DFPT is implemented in the QUANTUM ESPRESSO package,[11] within the plane-waves and pseudopotential approaches. The anharmonic scattering coefficients can be determined by the third-order derivative of the energy with respect to three phonon perturbations, characterized by the wave vectors $\mathbf{q}$, $\mathbf{q}'$, $\mathbf{q}''$. For the thermal transport problem, it is necessary to know these derivatives with respect to three arbitrary wave vectors (possibly $\mathbf{q} \neq \mathbf{0}$, $\mathbf{q}' \neq \mathbf{0}$, $\mathbf{q}'' \neq \mathbf{0}$), with the only condition $\mathbf{q} + \mathbf{q}' + \mathbf{q}'' = \mathbf{G}$, where $\mathbf{G}$ is a reciprocal lattice vector. In principle, these coefficients can be obtained within DFPT by using the so-called "$2n + 1$" theorem as formulated by Ref. 12. This theorem allows us to access the third derivative of the total energy by using only the first derivative of ground-state density and wave functions; contrary to the finite differences approach, we do not have to perform expensive supercell calculations.

The first implementations of the "$2n + 1$" approach were limited to the scattering of one zero-momentum phonon towards two phonons with opposite arbitrary momenta ($\mathbf{0}$, $-\mathbf{q}$, $\mathbf{q}$). Reference 13 implemented this approach for insulating and semiconducting materials. Later, Ref. 14 generalized the approach to metals and zero-gap materials. The ($\mathbf{0}$, $-\mathbf{q}$, $\mathbf{q}$) anharmonic coefficients can be computed within QUANTUM ESPRESSO,[11] using the D3 code, which was developed in Ref. 14. These coefficients can be easily used to compute the anharmonic broadening of a $\mathbf{q} = \mathbf{0}$ phonon (see, e.g., Ref. 15). By using a supercell approach, one can also compute the broadening of phonons having $\mathbf{q}$ commensurate with the supercell. However, the supercell approach (which was used in Refs. 8,9, and 15) can be computationally very demanding. Recently, Ref. 16 implemented a general code that treats three arbitrary phonons, ($\mathbf{q}$,$\mathbf{q}'$,$\mathbf{q}''$), although only for insulators/semiconductors. This was done within a proprietary non-publicly-available software.

Here, we have developed and implemented an extension of the D3 code of the QUANTUM ESPRESSO software to compute, within the DFPT "$2n + 1$" approach, the three-phonons anharmonic coefficients for three arbitrary wave vectors ($\mathbf{q}$,$\mathbf{q}'$,$\mathbf{q}''$) for insulators/semiconductors and also for metallic or zero-gap systems. The coefficients thus obtained can be used in a straightforward way to compute the anharmonic broadening of a phonon with an arbitrary wave vector $\mathbf{q}$ and the intrinsic thermal conductivity within the single-mode relaxation time approximation (SMA).[17] The first applications of the method

 ©2013 American Physical Society

are devoted to graphite, graphene, and graphene bilayer. Indeed, the thermal properties of these systems have attracted significant attention,[18,19] being sp^2 carbon systems excellent thermal semiconductors.

Section II describes the method. Section III reports the results and the discussion. Conclusions are summarized in Sec. IV.

II. METHOD

In Sec. II A, we provide the expressions for the phonon anharmonic broadening and for the phonon thermal conduction. In Sec. II B, the method is briefly described and we provide the relevant computational details. A more detailed description of the method is reported in Appendices A, B, and C.

A. Anharmonic decay and thermal transport

Let us consider the total energy for a crystal $\mathcal{E}^{\rm tot}(\{v_{\mathbf{R},s,\alpha}\})$, where $v_{\mathbf{R},s,\alpha}$ is the displacement from the equilibrium position of the s atom along the α Cartesian coordinate in the unit cell identified by the lattice vector $\mathbf{R}$. We define

$$u_{\mathbf{q},s,\alpha} = \frac{1}{N}\sum_{\mathbf{R}} e^{-i\mathbf{q}\cdot\mathbf{R}} v_{\mathbf{R},s,\alpha}, \tag{1}$$

where the sum is performed on the lattice vectors $\{\mathbf{R}\}$ and N is the number of cells involved in the summation. We define the dynamical matrix

$$D_2\begin{pmatrix} & \mathbf{q} & \\ s & & s' \\ \alpha & & \alpha' \end{pmatrix} = \frac{1}{N}\frac{\partial^2 \mathcal{E}^{\rm tot}}{\partial u_{-\mathbf{q},s,\alpha}\partial u_{\mathbf{q},s',\alpha'}}. \tag{2}$$

The angular frequency $\omega_{\mathbf{q},j}$ of a phonon with wave vector $\mathbf{q}$ and branch index j is obtained by solving

$$\sum_{s',\alpha'}\frac{1}{\sqrt{m_s m_{s'}}} D_2\begin{pmatrix} & \mathbf{q} & \\ s & & s' \\ \alpha & & \alpha' \end{pmatrix} z^{\mathbf{q},j}_{s',\alpha'} = \omega^2_{\mathbf{q},j} z^{\mathbf{q},j}_{s,\alpha}, \tag{3}$$

where z are the orthogonal phonon eigenmodes normalized in the unit cell and m_s is the atom mass. We define the three-phonon scattering coefficients as

$$V^{(3)}_{\mathbf{q}j,\mathbf{q}'j',\mathbf{q}''j''} = \frac{1}{N}\frac{\partial^3 \mathcal{E}^{\rm tot}}{\partial X_{\mathbf{q},j}\partial X_{\mathbf{q}',j'}\partial X_{\mathbf{q}'',j''}}, \tag{4}$$

where

$$\frac{\partial}{\partial X_{\mathbf{q},j}} = \sum_{s,\alpha}\sqrt{\frac{\hbar}{2m_s\omega_{\mathbf{q},j}}} z^{\mathbf{q},j}_{s,\alpha}\frac{\partial}{\partial u_{\mathbf{q},s,\alpha}}. \tag{5}$$

$V^{(3)}$ has the dimension of an energy and does not depend on N, while $X_{\mathbf{q},j}$ is adimensional. Because of the translational symmetry of the crystal, the coefficients $V^{(3)}$ from Eq. (4) are $\neq 0$ only when $\mathbf{q}+\mathbf{q}'+\mathbf{q}'' = \mathbf{G}$, where $\mathbf{G}$ is any reciprocal lattice vector.

With these definitions, the lifetime due to anharmonic phonon-phonon interaction, $\tau_{\mathbf{q}j}$, and the corresponding broadening $\gamma_{\mathbf{q}j}$ (full width at half maximum) of the phonon $(\mathbf{q}j)$ are[15]

$$\begin{aligned}\frac{1}{\tau_{\mathbf{q}j}(T)} = \gamma_{\mathbf{q}j}(T) = \frac{\pi}{\hbar^2 N_q}\sum_{\mathbf{q}',j',j''} &\left|V^{(3)}_{\mathbf{q}j,\mathbf{q}'j',\mathbf{q}''j''}\right|^2 \\ &\times[(1+n_{\mathbf{q}'j'}+n_{\mathbf{q}''j''})\delta(\omega_{\mathbf{q}j}-\omega_{\mathbf{q}'j'}-\omega_{\mathbf{q}''j''}) \\ &+2(n_{\mathbf{q}'j'}-n_{\mathbf{q}''j''})\delta(\omega_{\mathbf{q}j}+\omega_{\mathbf{q}'j'}-\omega_{\mathbf{q}''j''})],\end{aligned} \tag{6}$$

where T is the temperature, $n_{\mathbf{q}j}$ is the Bose-Einstein statistics occupation of phonon $(\mathbf{q}j)$, and $\delta(x)$ is the Dirac distribution. The sum is performed over a sufficiently fine grid of N_q $\mathbf{q}$ points in the Brillouin zone (BZ) and $\mathbf{q}'' = -\mathbf{q}-\mathbf{q}'$. $\tau_{\mathbf{q}j}$ and $\gamma_{\mathbf{q}j}$ depend on T only through the phonon occupations n.

The right-hand side of Eq. (6) is usually interpreted as the sum of scattering processes in which a phonon of wave vector $\mathbf{q}$ decays into two phonons $-\mathbf{q}'$, $-\mathbf{q}''$ [third line of Eq. (6)], or in which the phonon $\mathbf{q}$ coalesces with $-\mathbf{q}'$ and emits $-\mathbf{q}''$ [fourth line of Eq. (6)]. The energy conservation of the processes is guaranteed by the Dirac δ. One can also distinguish between normal and umklapp processes by choosing $\mathbf{q}$ and $-\mathbf{q}'$ such that they belong to the first BZ: the scattering is normal when also $\mathbf{q}'' = -\mathbf{q}-\mathbf{q}'$ belongs to the first BZ; on the contrary, when $\mathbf{q}''$ does not belong to the first BZ, the scattering is umklapp.

By knowing the anharmonic scattering coefficients, see Eq. (4), one can determine the lattice thermal conductivity within the framework of the Boltzmann transport equation (BTE) for phonons.[20] In general, an exact solution of the BTE is a difficult task; a commonly used approximation to the problem is the so-called single mode relaxation time approximation (SMA).[8,17] Within the SMA, the lattice thermal conductivity tensor becomes

$$\kappa_{\rm L}^{\alpha,\beta} = \frac{\hbar^2}{N_q\Omega K_{\rm B}T^2}\sum_{\mathbf{q}j} c^{\alpha}_{\mathbf{q}j}c^{\beta}_{\mathbf{q}j}\omega^2_{\mathbf{q}j}n_{\mathbf{q}j}(n_{\mathbf{q}j}+1)\tau_{\mathbf{q}j}. \tag{7}$$

Here, Ω is the volume of the unit cell, $K_{\rm B}$ is the Boltzmann constant, and $c^{\alpha}_{\mathbf{q}j}$ is the phonon group velocity of mode $(\mathbf{q}j)$ along Cartesian direction α: $c^{\alpha}_{\mathbf{q}j} = d\omega_{\mathbf{q}j}/(dq_\alpha)$. The SMA conductivity from Eq. (7) can be obtained in a straightforward way once the anharmonic lifetimes $\tau_{\mathbf{q}j}$ have been computed from Eq. (6). $\kappa_{\rm L}^{\alpha,\beta}$ is a 3×3 tensor, which takes into account the possible anisotropies and transversal conductance. However, in high-symmetry crystals, as graphene and graphite, the off-diagonal elements are zero, if two axes lie in the graphene plane. Moreover, in both graphene and graphite, the two in-plane xx and yy components are identical. The out-of-plane zz component is not defined in the bidimensional graphene systems, but it is meaningful in graphite.

The validity limits of the SMA are discussed in literature.[8,17] Here, we wish to remind that, for a generic material, the SMA is expected to be valid (that is, to provide the correct solution to the BTE) at room conditions and to break down only at very small temperatures (see, e.g., Ref. 7).

B. Density functional theory calculation

Calculations of the phonon properties are done within density functional perturbation theory[10] as implemented in Ref. 11. The third-order coefficients defined in Eq. (4) are computed using a code, which has been developed for the present work. This code has been written on the top

of a previous less general implementation available within the QUANTUM ESPRESSO package: the D3 code, which was implemented in Ref. 14. The method is a straightforward generalization of the one from Ref. 14, it is described in detail in Appendices A and B.

We use local density approximation and the carbon atom is described by a norm-conserving pseudopotential, which includes four electrons in valence. The plane-waves kinetic energy cutoff is 90 Ry. For all the systems, the in-plane lattice parameter is $a = 2.44$ Å, which is the theoretical equilibrium value for graphite. For graphite, we use $c/a = 2.664$. This value, which is only slightly different from the experimental value $c/a = 2.727$, is chosen phenomenologically to accurately reproduce the low-frequency phonon dispersion along the **Γ**-**A** direction (see the discussion below). For graphene, the periodic replicas of the planes are spaced along the z direction with 7 Å of vacuum. The two layers of the graphene bilayer are spaced with the interplanar distance of bulk graphite; periodic images are then spaced with 7 Å of vacuum.

The computational parameters are listed in Appendix D. We remind here that the electronic integration has to be done with a small value of smearing (and a consequent fine-grained **k**-point grid) due to the presence of a Kohn anomaly for the highest optical branch near **K** (usually called TO).[23] The phonon frequencies $\omega_{\mathbf{q}j}$ and the third-order coefficients $V^{(3)}$, used in Eqs. (6) and (7), are calculated in a slightly different way. On one hand, phonon energies are corrected using an *ad hoc* procedure (based on DFT + GW renormalization of the electron-phonon interaction as in Ref. 24, see Appendix D). This correction affects only the TO branch, it does not touch the other branches, and it provides better agreement with measurements, see Fig. 1. On the other hand, the third-order coefficients are computed within standard (less precise) DFT. The use of these two different procedures for the $\omega_{\mathbf{q}j}$ and $V^{(3)}$ calculations is not consistent. However, this should not affect the results in a major way. Indeed, the phonon broadening results from a sum on different processes, which are selected by energy conservation implemented by the two Dirac δ in Eq. (6). The intensity of the processes is then proportional to the square of the $V^{(3)}$ coefficients. Consequently, the computational accuracy of $\omega_{\mathbf{q}j}$ and that of the $V^{(3)}$ coefficients affect the result in a very different way. An error in the phonon dispersion can affect the lifetime in a nonpredictable way and, thus, a special care should be taken into finding the best possible description of the phonon dispersion. The same care is not strictly necessary for the third-order calculations.

Figure 1 compares measured with calculated phonon dispersions for graphite. Notice that plain DFT calculations do not provide a satisfactory description of the highest optical TO branch near **K**, while DFT + GW ones do much better. The lower panel of Fig. 1 shows in detail the low-frequency dispersion. This region is characterized by the splitting of the acoustic phonon branches of the two graphene planes in the graphite unit cell. These branches are particularly sensitive to the actual value of c/a. In particular, in that region, by changing the lattice parameters from $c/a = 2.664$ (which is the value used throughout the paper) to 2.727, the value of the phonon branches changes by almost 14%.

Actual DFT calculations are done on a relatively coarse grid of **q** wave vectors, described in Appendix D. The dynamical

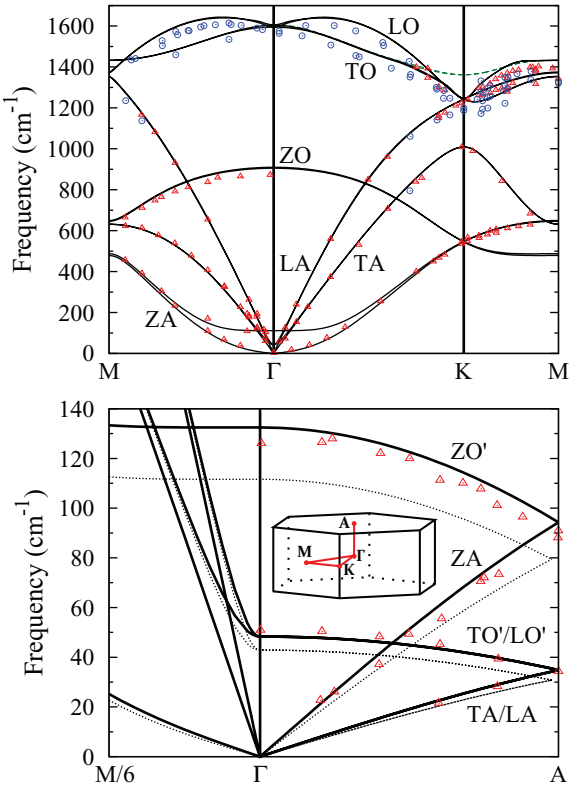

FIG. 1. (Color online) Graphite phonon dispersion. Symbols are measurements from Refs. 21 and 22. Lines are calculations. (Top) TO optical branches are plotted two times. The solid (black) lines include GW corrections of the electron-phonon interaction. On the contrary, the dashed (green) lines are done using standard DFT and they are shown only for comparison. (Bottom) Solid lines are done by using $c/a = 2.664$; dashed lines are done with $c/a = 2.727$ and they are shown only for comparison. In the inset, we recall the high-symmetry points naming convention. In both panels, the solid lines correspond to the calculations used throughout the paper.

matrices and the third-order coefficients, necessary to compute the broadening and the thermal conductivity [see Eqs. (6) and (7)], are then obtained on a finer grid via the Fourier interpolation technique described in Appendix C. Equations (6) and (7) are evaluated by performing the sum over a discrete grid of **q** points and by substituting the $\delta(x)$ with the Gaussian function characterized by an artificial smearing χ. This approximation is valid as long as χ is smaller than the thermodynamic fluctuation, which is of order $K_B T$. The grids and the χ values are specified in Appendix D. Here, we just remark that the results shown in Secs. III A and III B are obtained using a particularly fine-grained sampling. This is only necessary to produce the very sharp features, which are present in the broadening of the higher optical bands or to produce the correct behavior of the broadening of the acoustic branches in the vicinity of **Γ**. Indeed, a much coarser grid is sufficient for most applications, included those described in Sec. III C.

III. RESULTS AND DISCUSSION

This section reports and describes the results. Section III A analyzes the anharmonic phonon broadening in the graphene

monolayer. Special relevance is given to the three acoustic branches, which are the most important for the thermal transport. Section III B analyzes the broadening in graphene bilayer and graphite. Section III C is dedicated to thermal transport.

A. Graphene phonon broadening

Figure 2 shows the calculated graphene phonon dispersion, the respective anharmonic broadening and the vibrational density of states (VDOS). The branches are labeled in the usual way.[25] There are three acoustic branches (ZA, TA, LA) and three optical branches (ZO, TO, LO). ZA and ZO correspond to an atomic motion perpendicular to the graphene plane (z direction), all the other branches are polarized parallel to the plane. In the vicinity of $\mathbf{\Gamma}$, TA and TO are quasitransverse, while LA and LO are quasilongitudinal. In the following, these labels will be used to classify the branches all along the high-symmetry lines (as in Fig. 2), although this distinction is not meaningful for an arbitrary wave vector in the Brillouin zone (BZ). Because of symmetry, the modes perpendicular polarized (ZA and ZO) are separated from the others all over the BZ. Moreover, the TA branch is always well separated from the other parallel polarized branches (labeled as P_H). In Fig. 2, we can, thus, separate the VDOS in three distinct components labeled as Z, TA, and P_H. The two-dimensional character of the phonon dispersion is associated with some specific features. The ZA branch is quadratic near $\mathbf{\Gamma}$ and, thus, in the limit $\omega \to 0$, the VDOS does not go to zero (see Fig. 2). The presence of a local maximum in the phonon dispersion (as the one at 1008 cm^{-1} for the TA branch near **K** or the one at 904 cm^{-1} for the ZO one near $\mathbf{\Gamma}$) is associated with a step in the VDOS. The presence of a saddle point in the dispersion (as those at 477, 631, 643, and 1432 cm^{-1} at the **M** point) is associated with a sharp peak in the VDOS.

Figure 3 reports in more detail the calculated anharmonic phonon broadening, along high-symmetry lines, and its decomposition into the different allowed decay channels. For symmetry reasons, the z-polarized branches can only decay toward one Z and one non-Z phonons.[26,27] The other bands can only decay towards two phonons, which are either both or neither z polarized. The two most striking features in Figs. 2 and 3 are the small q behavior of the acoustic branches and the highly nonuniform behavior of the broadening.

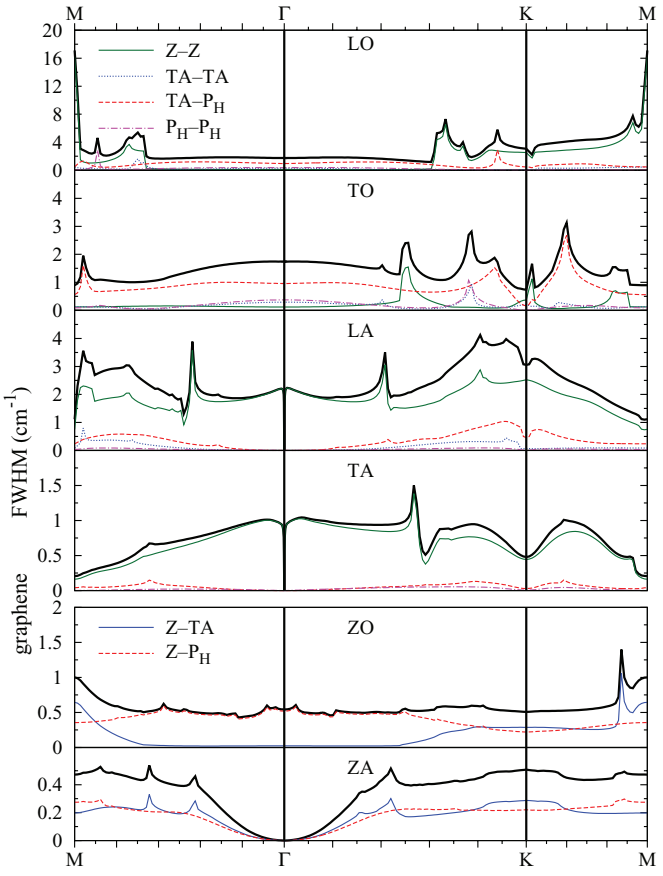

FIG. 3. (Color online) Graphene anharmonic phonon broadening (FWHM) at 300 K, for each phonon branch (labeled as in Fig. 2), along high-symmetry lines. The total broadening (solid thick line) is decomposed depending on the character of the final states, which are labeled as Z, TA, and P_H (see the text), e.g., TA-P_H corresponds to a decay involving one TA and one P_H phonons.

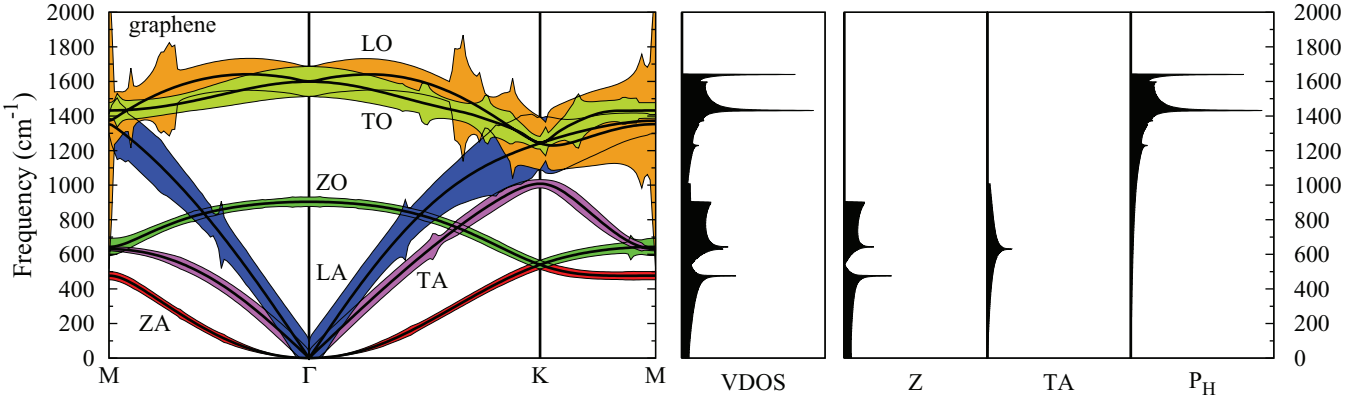

FIG. 2. (Color online) Calculated graphene phonon dispersion. Each phonon branch is represented with a variable-width filled band: the graphical width is equal to the respective anharmonic broadening at 300 K, expressed in cm^{-1} and magnified by a factor 100. The vibrational density of states (VDOS) is also shown, together with its decomposition over groups of disentangled branches labeled as Z (corresponding to the ZA and ZO branches), TA and P_H (corresponding to LA, TO, and LO).

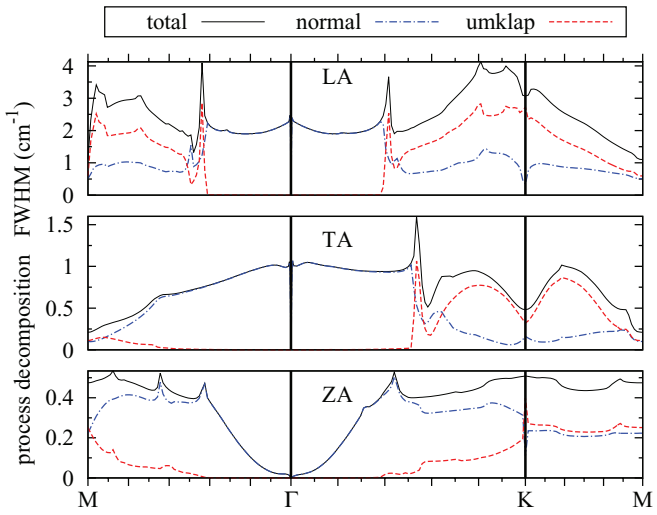

FIG. 4. (Color online) Graphene anharmonic phonon broadening for the three acoustic branches at 300 K (same data as in Fig. 3): the broadening is decomposed in two components, which are due, respectively, to normal and umklapp processes.

First, we remind that in a three-dimensional isotropic crystal, all the three acoustic branches are linearly dispersive and one expects to observe for $q \to 0$ a vanishing broadening. On the contrary, at finite temperature, both TA and LA branches of the two-dimensional graphene have a nonzero broadening in the $q \to 0$ limit. This behavior is due to a decay process in which a TA (or LA) phonon decays into two phonons both in the ZA branch, Fig. 3. This decay is entirely due to normal scattering. This can be seen in Fig. 4, where the broadening of the acoustic branches is decomposed into the two components which are due, respectively, to normal and umklapp processes, as defined in Sec. II A. Actually, one can demonstrate[9] that in general, when a linearly dispersive phonon decays into two quadratically dispersive phonons, the broadening is nonvanishing in the $q \to 0$ limit because of energy and momentum conservation. Moreover, the quadratically dispersive ZA branch has a broadening, which is itself quadratic in q around $\mathbf{\Gamma}$. The ZA broadening is due to a normal decay in which the ZA phonon decays into one ZA phonon and one linearly dispersive, TA or LA, phonon. Again, one can demonstrate that, in general, when a quadratically dispersive phonon decays into one quadratically and one linearly dispersive phonons, the broadening vanishes quadratically in the $q \to 0$ limit. We remark that here, the anharmonic broadening has been computed by summing over an extremely fine reciprocal-space grid (see Appendix D). This is necessary in order to reproduce correctly the anomalous behavior of the LA and TA broadenings for small q. Far from $\mathbf{\Gamma}$, the details of the broadening can be correctly reproduced by using a much coarser grid and a larger χ.

The existence of a finite broadening at small q for the TA and LA acoustic branches is problematic. Indeed, the concept itself of phonon is meaningful only when $\omega/\gamma > 1$, being γ the broadening (i.e., the inverse of the phonon lifetime). From the present calculations, the condition $\omega/\gamma > 1$ is satisfied for both the TA and LA branches for $q > \overline{q}$, with $\overline{q} = 0.5 \times 10^{-4} 2\pi/a_0$, a_0 being the in-plane lattice spacing. Thus for $q < \overline{q}$, the TA or LA frequency can become smaller that the broadening. In this region, the present treatment is, obviously, not valid (see the discussion in Ref. 9) and a proper treatment of the phenomenon is beyond the present scope. In practice, however, $q < \overline{q}$ represents a tiny portion of the Brillouin zone (the corresponding region in Figs. 2 and 3 has a width of the order of the thickness of the vertical line passing through $\mathbf{\Gamma}$). As a consequence, we can assume that the properties obtained as a sum over the Brillouin zone [such as the thermal conductivity of Eq. (7)] are not affected by a major error.

Concerning the global appearance of Figs. 2 and 3, the many sharp peaks in the broadening can be ascribed to different mechanisms. Those in the high-energy part of the spectrum are, in general, associated with peaks in the VDOS: when one or both of the final states [i.e., of the states that meet the energy and momentum conservation requirements in Eq. (6)] produce a peak in the VDOS, there the broadening will typically exhibit a peak. For example, the large scattering probability, predicted for the $\mathbf{M}$ point on the LO branch (1373 cm^{-1}), corresponds to a decay toward a ZO phonon close to $\mathbf{\Gamma}$ (904 cm^{-1}) and a ZA phonon close to $\mathbf{M}$ (477 cm^{-1}). As the VDOS, Fig. 2, has maximum in both regions, this transition is particularly favored. On the other hand, for $\mathbf{q} \gtrsim 0.66\mathbf{M}$ (along the $\mathbf{\Gamma}$-$\mathbf{M}$ direction) or for $\mathbf{q} \gtrsim 0.62\mathbf{K}$ (along $\mathbf{\Gamma}$-$\mathbf{K}$), the LO broadening displays a sudden increase. This is because, for these wave vectors, the LO energy becomes small enough to activate the decay channel towards the ZO branch. (At $\mathbf{q} \sim 0.66\mathbf{M}$ and $\mathbf{q} \sim 0.62\mathbf{K}$, the LO phonon decays into a ZO with the same wave vector and a ZO with $\mathbf{q} \sim \mathbf{\Gamma}$.) We remark that the presence of sharp peaks, which are essentially determined by energy and momentum conservation in the decay process, implies that even a small change in the phonon dispersion used in the calculation could induce significant differences in the calculated broadening.

Concerning the three acoustic branches, the broadening near $\mathbf{\Gamma}$ is almost entirely due to normal scattering, see Fig. 4. The peaks which are observed at $\mathbf{q} \gtrsim 0.44\mathbf{M}$ and $\mathbf{q} \gtrsim 0.41\mathbf{K}$ for the LA branch, and at $\mathbf{q} \gtrsim 0.65\mathbf{M}$ and $\mathbf{q} \gtrsim 0.54\mathbf{K}$ for the TA one, are associated with the activation of umklapp scattering towards the ZA phonons. To have a more comprehensive view, Fig. 5 reports the broadening in the entire Brillouin zone. The TA and LA branches exhibit a feature-rich behavior in a wide region, far from $\mathbf{\Gamma}$, which roughly starts at about halfway to the first BZ edge. In this region, the anharmonic decay presents a component of umklapp processes, which is absent in the vicinity of $\mathbf{\Gamma}$, where the scattering is almost entirely normal. On the other hand, the ZA broadening is relatively featureless and isotropic; it is quadratic in $\mathbf{q}$ in the center of the first BZ then it saturates and remains roughly constant.

1. Phonon mean-free path

An alternative way to represent the effect of the phonon broadening is to plot the single-phonon mean-free path (MFP):

$$\lambda_{\mathbf{q}j} = \tau_{\mathbf{q}j} |\mathbf{c}_{\mathbf{q}j}|, \tag{8}$$

where $\mathbf{c}_{\mathbf{q}j}$ is the phonon group velocity and $\tau_{\mathbf{q}j}$ is the phonon lifetime, from Eq. (6). In Fig. 6, we have plotted the MFP

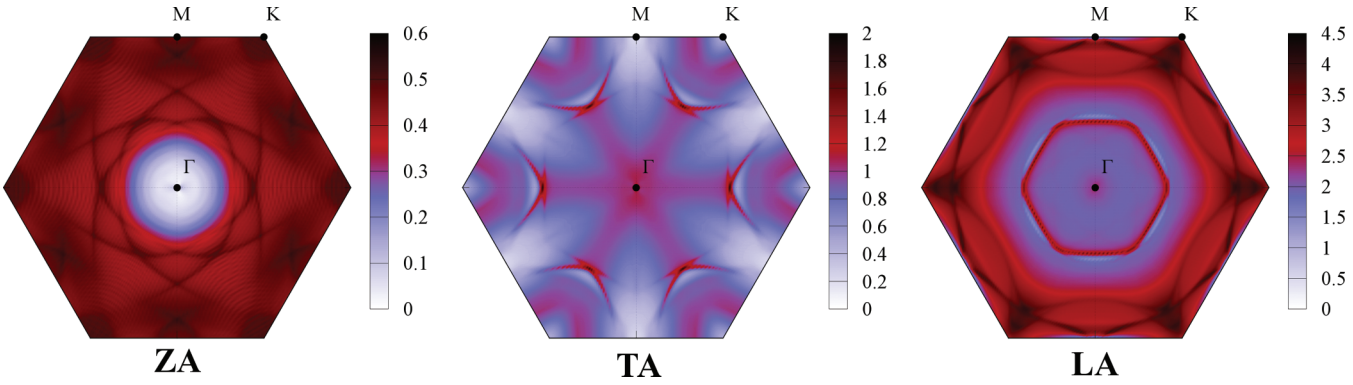

FIG. 5. (Color online) Graphene anharmonic phonon broadening (FWHM, in cm^{-1}) at 300 K, for the three acoustic branches, over all Brillouin zone.

at 300 K for the three acoustic branches. The MFP for the TO and LO bands is of order 100 nm or smaller. We have verified that it does not get substantially higher at lower temperatures, except in the vicinity of $\mathbf{\Gamma}$ where it diverges at 0 K. At room temperature, the MFP of the ZA bands is one order of magnitude larger, i.e., of order 1 μm, in the center region of the BZ. Furthermore, it increases as $1/T$ when temperature decreases. Obviously, especially at small temperatures, when the intrinsic anharmonic MFP is too big, other effects (typically the scattering on the borders of the sample) become important and limit the value of the MFP. We remark that the MFP of acoustical phonons is only one order of magnitude smaller than the typical dimensions of high-quality graphene samples. It is, also, definitely larger than the transverse dimension of graphene nanoribbons. This result suggests that ballistic phonon-driven conductance could play a relevant role in this kind of systems.

2. *Temperature dependence*

The intrinsic anharmonic broadening of a specific phonon ($\mathbf{qj}$) has, in general, a typical dependence of the temperature T: it is almost constant below a certain characteristic temperature θ^{s}, then it rapidly becomes linear in T. Such a behavior is reproduced by Eq. (6). A quadratic dependence on T can be observed experimentally only at relatively high T and it is due to terms of order higher than those included in Eq. (6).[28]

From Eq. (6), one can check that

$$\lim_{T\to\infty} \gamma_{\mathbf{q}j}(T) = \alpha_{\mathbf{q}j} T + \mathcal{O}(1/T), \tag{9}$$

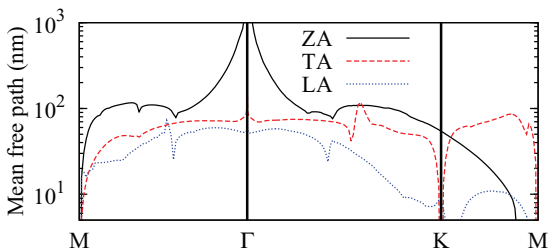

FIG. 6. (Color online) Phonon mean-free path for the three acoustic branches in graphene at 300 K.

where

$$\alpha_{\mathbf{q}j} = \frac{\pi K_{\mathrm{B}}}{\hbar^3 N_q} \sum_{\mathbf{q}',j',j''} \left|V^{(3)}_{\mathbf{q}j,\mathbf{q}'j',\mathbf{q}''j''}\right|^2 \times \left[\left(\frac{1}{\omega_{\mathbf{q}'j'}} + \frac{1}{\omega_{\mathbf{q}''j''}}\right)\delta(\omega_{\mathbf{q}j} - \omega_{\mathbf{q}'j'} - \omega_{\mathbf{q}''j''}) + 2\left(\frac{1}{\omega_{\mathbf{q}'j'}} - \frac{1}{\omega_{\mathbf{q}''j''}}\right)\delta(\omega_{\mathbf{q}j} + \omega_{\mathbf{q}'j'} - \omega_{\mathbf{q}''j''})\right] \tag{10}$$

does not depend on T. One can thus be tempted to approximate the overall dependence on T of the broadening γ by

$$\gamma_{\mathbf{q}j}(T) \simeq \tilde{\gamma}_{\mathbf{q}j}(T) = \alpha_{\mathbf{q}j}\theta^{\mathrm{S}}_{\mathbf{q}j}\coth\left(\frac{\theta^{\mathrm{S}}_{\mathbf{q}j}}{T}\right), \tag{11}$$

where coth is the hyperbolic cotangent, $\theta^{\mathrm{S}}_{\mathbf{q}j} = \gamma_{\mathbf{q}j}(0)/\alpha_{\mathbf{q}j}$, and $\gamma_{\mathbf{q}j}(0)$ is the $T = 0$ broadening from Eq. (6). Indeed, $\tilde{\gamma}$ from Eq. (11) is almost constant for $T \ll \theta^{\mathrm{S}}$ and tends to $\gamma(0)$ for $T \to 0$. Moreover, $\tilde{\gamma}(T) = \alpha T + \mathcal{O}(1/T)$ for $T \gg \theta^{\mathrm{S}}$. To check the validity of this approximation [see Eq. (11)], we systematically computed the graphene broadening for different phonons in the temperature range between 0 and 1500 K, using Eq. (6). These results are reasonably well reproduced by Eq. (11) with an error less than 5%.

As a consequence, for a given phonon mode ($\mathbf{q}j$), the knowledge of the two corresponding parameters θ^{S} and α is enough to determine the overall temperature behavior of the broadening by using Eq. (11). The two parameters can be extracted from Fig. 7 for the graphene acoustic branches, along high-symmetry lines.

Finally, the broadening of the LA and TA branches can be fitted with an isotropic function of $q = |\mathbf{q}|$ and of T of the form

$$\gamma(q,T) = qB\coth\left(\frac{qA}{T}\right). \tag{12}$$

By defining $b_0 = \frac{2\pi}{a_0}$, where a_0 is the cell parameter, we have for the LA band, $B_{\mathrm{LA}} = 4.58\ \mathrm{cm}^{-1}/b_0$ and $A_{\mathrm{LA}} = 694\ \mathrm{K}/b_0$; for the TA band, $B_{\mathrm{TA}} = 0.805\ \mathrm{cm}^{-1}/b_0$ and $A_{\mathrm{TA}} = 241\ \mathrm{K}/b_0$. These fitted parameters reproduce the computed linewidth with an error of generally less than 10% for $q < 0.40b_0$ (smaller for higher temperature and lower $|\mathbf{q}|$). For the ZA band, $\theta^{\mathrm{s}} = 0$

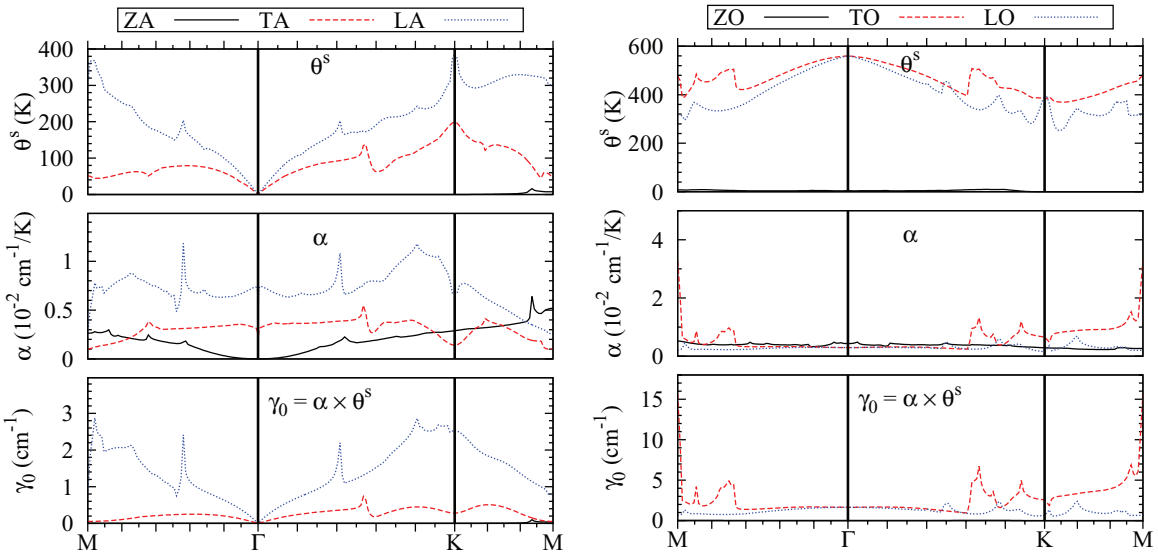

FIG. 7. (Color online) θ^S and α parameters (defined in the text) for the graphene acoustic (left) and optical (right) branches. For a given phonon mode, the temperature dependence of the anharmonic broadening can be approximated by $\gamma(T) \simeq \alpha\theta^S \coth(\theta^S/T)$, where θ^S and α are the parameters corresponding to that phonon. θ^S is a characteristic temperature and α is the high-temperature slope of $\gamma(T)$. γ_0 is the $T = 0$ K broadening.

can be assumed, resulting in this simple fitting function:

$$\gamma(q,T) = Bq^2T\,. \tag{13}$$

Taking $B_{ZA} = 25.9 \times 10^{-3}$ cm$^{-1}/b_0^2$, we reproduce the value of linewidth to 10% accuracy in the range $q < 0.25b_0$, except for systematically underestimating it in the very small **q** region where it is negligible ($\gamma < 10^{-5}$ cm^{-1}).

B. Graphite and bilayer graphene

We now discuss the anharmonic broadening in graphite and graphene bilayer. Each of the six phonon branches of the graphene monolayer splits into two branches for both graphite and graphene bilayer. The three acoustic branches of graphene (ZA, TA, LA) split into three acoustic (ZA, TA, LA) and three quasiacoustic branches (ZO′, TO′, LO′). The quasiacoustic branches are almost degenerate with their respective acoustic ones, except in the vicinity of the **Γ**-**A** line. The remaining six optical branches are pair-wise quasidegenerate in the entire Brillouin zone, and they will be referred in pairs simply as ZO, TO, and LO or, in some cases as ZO^1, ZO^2, etc. This notation does not hold along the **Γ**-**A** line in graphite, as degeneracy changes. It is, however, still possible to name the branches by continuity below 600 cm^{-1}.

Figure 8 shows a general view of the calculated phonon dispersion and broadening in bulk graphite and graphene bilayer. Figures 9 and 10 compare the broadening of the acoustic and quasiacoustic branches of, respectively, graphite and bilayer graphene with those of the single-layer graphene. Figure 11 shows in more detail the low-frequency region. In the high-energy part of the spectrum, graphite and graphene monolayer and bilayer are almost indistinguishable, see Fig. 8, meaning that, also in graphite, the physics is ruled by the two-dimensional character of the phonon dispersion. Some of the graphene sharp features are a slightly broader in graphite due to the out-of-plane phonon dispersion acting like an effective smearing. The most striking differences between three-dimensional bulk graphite and two-dimensional graphene monolayer and bilayer are associated with the acoustic and quasiacoustic branches.

First, we remind that, in graphene, the vibrational density of states (VDOS in Fig. 2) has a finite constant value for

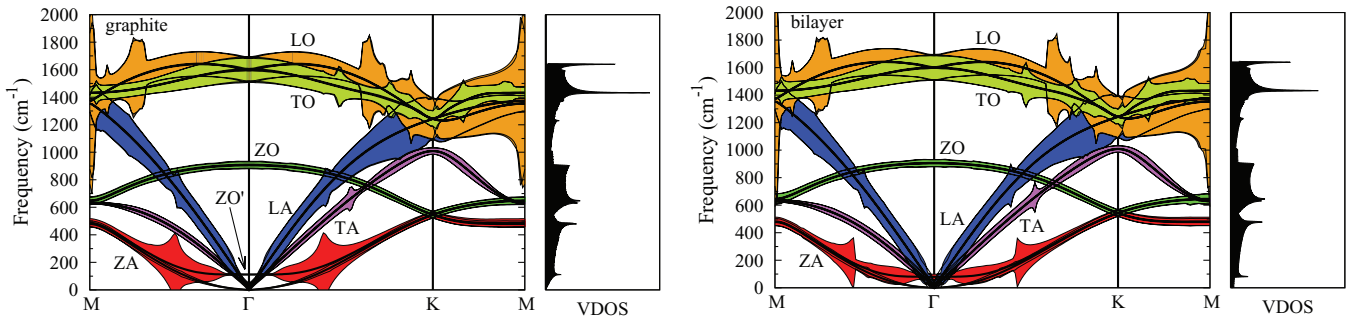

FIG. 8. (Color online) Graphite and graphene bilayer: calculated phonon dispersion widened by the anharmonic broadening (FWHM ×100) at 300 K.

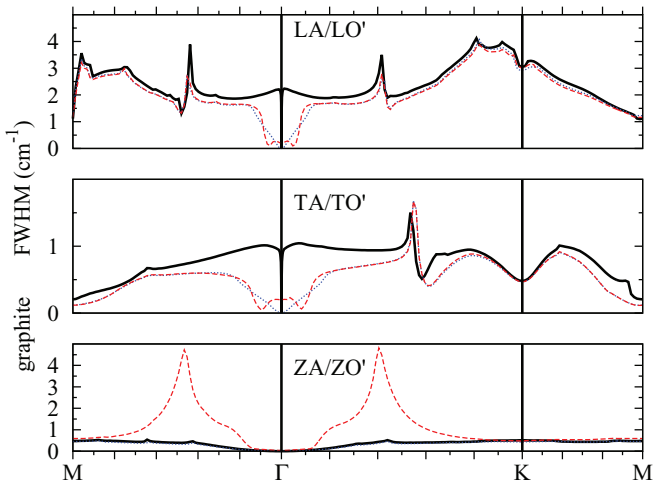

FIG. 9. (Color online) Anharmonic phonon broadening (FWHM) at 300 K. Graphene acoustic branches (solid line) are compared with the corresponding graphite acoustical (dotted) and quasiacoustical (dashed) ones.

energies approaching zero. This is because the ZA branch has a quadratic dispersion (not linear as usual) and the VDOS is calculated in a two-dimensional BZ. On the contrary, in graphite, the VDOS goes to zero almost linearly for energies going to zero, Fig. 8. This happens in spite of the fact that in graphite, when the out-of-plane component $q_z = 0$, the ZA branch is not very different from the graphene one. In particular, on the scale of Fig. 8, the graphite ZA branch (for $q_z = 0$) appears quadratic as the graphene one from Fig. 2. However, for graphite, the VDOS is calculated in a three-dimensional BZ and the $q_z = 0$ phonons have an infinitesimal weight. Also, notice in the graphite VDOS, the presence of a peak at 132 cm^{-1} corresponding to the ZO′ frequency at $\mathbf{\Gamma}$. This peak and this phonon do not have a correspondence in graphene. Finally, from Fig. 8, the bilayer VDOS has a finite constant value for zero energy (as for the monolayer), and it also shows the ZO′ peak at 94 cm^{-1} (as in graphite).

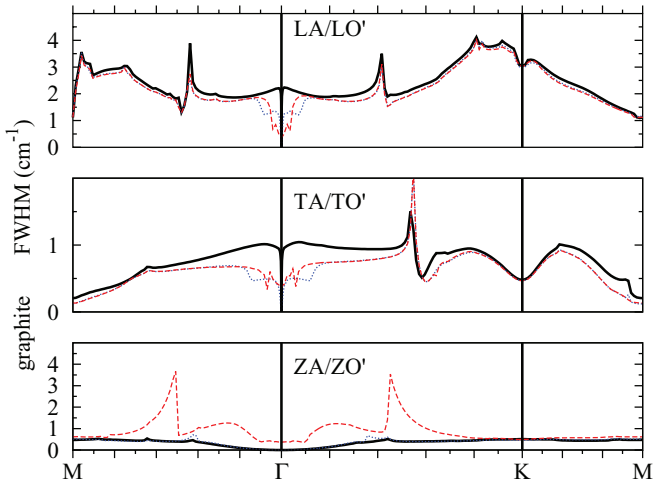

FIG. 10. (Color online) Anharmonic phonon broadening (FWHM) at 300 K. Graphene monolayer acoustic branches (solid line) are compared with the corresponding bilayer acoustical (dotted) and quasiacoustical (dashed) ones.

Let us consider the broadening of the LA and TA branches in Fig. 9. As already said, in graphene, these broadenings do not vanish for $q \to 0$ and, for small q, they are relatively constant over a wide range of q values (e.g., for the LA mode we are considering the region with $\mathbf{q} < 0.4\mathbf{M}$ and $\mathbf{q} < 0.4\mathbf{K}$ in Fig. 9). This "plateau" is due to normal scattering towards the ZA phonons and its characteristics stem for the fact that the ZA dispersions are quadratic and that the integration [the sum in Eq. (6)] is done on a two-dimensional BZ. On the contrary, for three-dimensional graphite, the broadening of both LA and TA modes vanishes for $q \to 0$. It is remarkable, however, that the graphite broadening still presents a normal scattering plateau, similar to the one of graphene, for sufficiently large q. This is particularly evident for the LA mode for $\mathbf{q} > 0.2\mathbf{M}$ and $\mathbf{q} > 0.2\mathbf{K}$ in Fig. 9. The LA and TA broadenings in bilayer graphene, Fig. 10, are rather more similar to the graphite one than to the graphene ones, indicating that for a higher number of layers, the broadening should rapidly converge to the bulk graphite one. Note that graphene bilayer presents nonvanishing broadening of the TA and LA bands at $\mathbf{\Gamma}$, its magnitude being about half for bilayer than for graphene.

Finally, let us consider the z-polarized branches. The ZA broadening in graphite is similar to the graphene one. On the other hand, the ZO′ broadening of graphite is much larger than the ZA one, in spite of the fact that the ZO′ and ZA branches are strictly related. Particularly striking is the sudden increase in the ZO′ broadening for certain values of $\mathbf{q}$ in the vicinity of $\mathbf{\Gamma}$ (e.g, for $\mathbf{q} = 0.47\mathbf{M}$ along the $\mathbf{\Gamma M}$ direction). This peak of the broadening is due to the decay of a ZO′ phonon, having a finite wave vector $\mathbf{q}$ into a ZA phonon near $\mathbf{q}$ and a LO′ (or TO′) phonon near $\mathbf{\Gamma}$. This kind of decay is possible only when the energy difference between the ZO′ and the ZA is equal or smaller than the energy of the LO′ and TO′ at $\mathbf{\Gamma}$ (the LO′ and TO′ are degenerate at $\mathbf{\Gamma}$), see Fig. 11. This condition is verified only for $\mathbf{q}$ sufficiently far from $\mathbf{\Gamma}$. Thus by increasing q, the sudden availability of this new decay channel produces the peak in the broadening. Finally, for the bilayer, the ZO′ broadening presents a structure which is not fundamentally different from the one in graphite.

C. Thermal transport

The intrinsic anharmonic thermal conductivity κ_L has been computed within the single mode time relaxation approximation using Eq. (7). For the two-dimensional materials (graphene monolayer and bilayer), we have used the convention that the volume Ω in Eq. (7) is the surface planar unit cell multiplied by the interlayer distance of graphite, 3.32 Å. Figure 12 reports the thermal conductivity and its decomposition into different branch contributions. In the temperature range considered, the conductivity is almost entirely due to the acoustic and the quasiacoustic branches. Calculations of Fig. 12 are done for $T > 200$ K. Below that temperature, converged results can be obtained only by using a much finer q-points grid than those presently used.

Let us, first, consider graphene. From Fig. 12, the ZA contribution increases by decreasing the temperature (actually, it diverges for $T \to 0$), while the LA and TA contributions

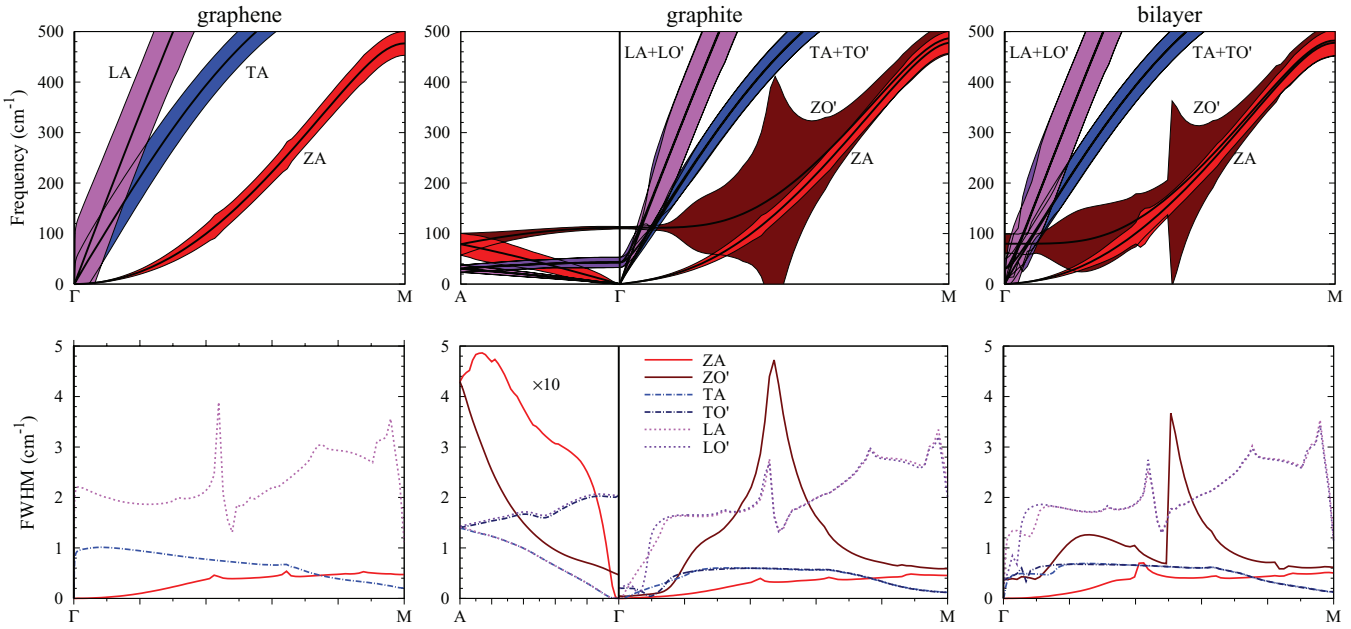

FIG. 11. (Color online) Phonon dispersion and anharmonic broadening of the acoustic and quasiacoustic branches of graphene, graphite, and graphene bilayer. The upper panels show the lower part of the phonon dispersion as in Figs. 2 and 8. The lower panels show the FWHM at 300 K. The values in the **A**-**Γ** section for graphite are magnified by a factor 10.

are nonmonotonic and reach a maximum near 300 K. The difference in the two behaviors can be understood by considering that, for small T, the phonons mostly occupied have small q, and that, for $q \to 0$, the anharmonic broadening [the inverse of the τ appearing on the right-hand side of Eq. (7)] of the ZA mode goes to zero at any T. This is not the case for the broadening of the TA and LA branches, see Fig. 3. Now, let us compare in Fig. 12 graphene with graphite. The ZA contribution in graphene corresponds, in graphite, to the two separate contributions ZA and ZO′. These two are quite different already at room temperature. Below room temperature, the ZA increases and diverges for $T \to 0$ (as for the ZA in graphene), while the ZO′ does not. The TA contribution in graphene corresponds to the TA and TO′ ones in graphite. Above 200 K, the TA and TO′ contributions are almost indistinguishable, in spite of the fact that only the TA branch is actually acoustical. Important differences between TA and TO′ contributions appear only below 50 K (not shown). The same considerations hold for the LA LO′ couple. By comparing in Fig. 12 graphite with the bilayer, above 200 K, the overall behavior of the two systems is relatively similar, in spite of the different dimensionality. Indeed, in the same temperature range, the total conductivity of two-dimensional graphene mono- and bilayers and that of three-dimensional graphite are relatively very similar, Fig. 13, with a difference between graphene and graphite of less than 10%.

Figure 12 also reports the measured in-plane thermal conductivity. This is done only for bulk graphite, because of the abundance of experimental data. At present, experimental measurements on graphene exist only for small samples, where border effects are important, consequently, the range of measured values is large and the number of samples in temperature limited.[18] From Fig. 12, the calculated graphite conductivity (which is obtained within the SMA) grossly underestimates the measured one, by about a factor of two. It is unlikely that this disagreement is due to density functional

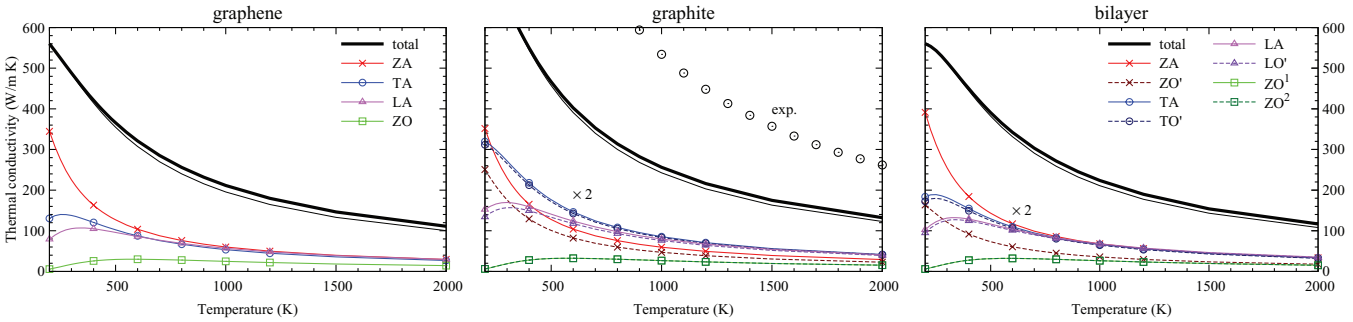

FIG. 12. (Color online) In-plane thermal conductivity obtained within SMA (thick solid line) and its decomposition into the contributions due to different phonon branches. The figure shows only the contributions from a subset of the most relevant phonon branches. The sum of these partial contributions is the thin solid line close to the total conductivity. In order to compare more easily the curves, the single branch contributions of graphite and bilayer are scaled by a factor 2. Dots are experimental data from Ref. 29.

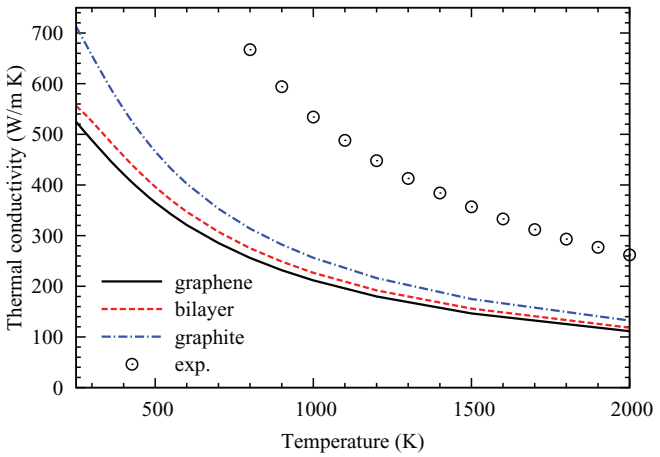

FIG. 13. (Color online) In-plane thermal conductivity calculated within the SMA for graphene single and bilayer and bulk graphite. Measurements (exp.) are done on graphite and are from Ref. 29.

theory. Indeed, DFT reproduces accurately the measured graphite phonon dispersion, see Fig. 1, suggesting that the most important quantities used in Eq. (7) are correct. On the other hand, as already explained at the end of Sec. II A, the thermal conductivity calculated according to Eq. (7) derives from the single mode relaxation time approximation and does not from an exact solution of the transport equation. Indeed, according to Refs. 27 and 30, the SMA can not be used to properly describe the in-plane thermal conductivity in graphitic materials and the exact solution of the Boltzmann transport equation is required. However, the results of Refs. 27 and 30 are obtained by using a semiempirical interatomic potential and a direct comparison with the present results is not meaningful. Further investigation on this point is required.

We now consider the thermal conductivity along the z axis, perpendicular to the graphene planes. Figure 14 shows calculations and compares them with measurements. The quasitotality of the conduction is due to the acoustic and quasiacoustic phonons polarized along z and, as expected,

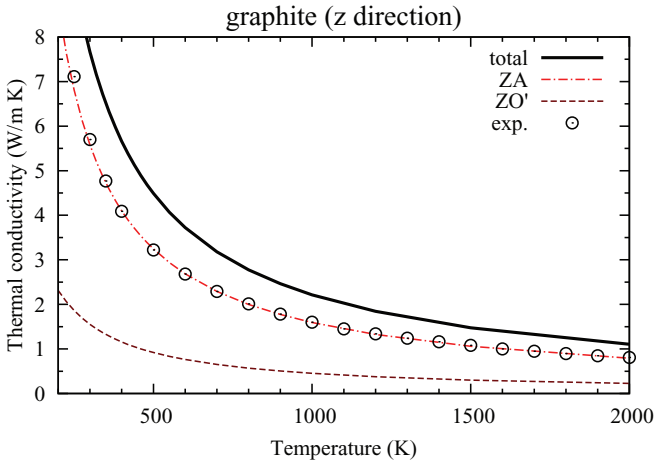

FIG. 14. (Color online) Thermal conductivity of graphite along the direction orthogonal to the planes and its decomposition into different phonon contributions. Measurements (exp.) are from Ref. 29 and should be compared with the line labeled as "total."

the conduction is much smaller than the in-plane one. The transport in plane and the one along z are quite different. The phonons relevant for the z conduction have much smaller velocity and are localized around γ in reciprocal space. Indeed, only phonons with a nonzero dispersion along the z axis can conduct since they have a nonzero velocity and, thus, can give a contribution to the sum in Eq. (7). These phonons belong to a small region surrounding the $\mathbf{\Gamma}$-$\mathbf{A}$ line. If we only integrate the contribution from a zz-oriented $\mathbf{q}$-space cylinder centered around Γ, we estimate that at 300 K, the central 20% of the WS cell contributes about 85% of the transverse transport, but only about 40% of the in-plane transport.

We also remark that the z conduction is extremely sensitive to the value of the c/a lattice parameter. Indeed, a small change in c/a results in a systematic increase or decrease of the frequencies of all the phonons relevant for the transport along z, see Fig. 1. Moreover, a systematic rescale of phonon frequencies by a certain factor λ results in a rescale of the conduction by a factor which can be much bigger than the initial λ [see Eq. (7)]. The agreement with measurements from Fig. 14 is satisfactory; the theoretical calculations slightly overestimate the experimental value, as we expect since we are omitting isotopic effects. We judge it compatible with the assumption that the SMA correctly describes the thermal transport along the z axis.

IV. CONCLUSIONS

We have developed and implemented a generic method for the calculation of anharmonic three-phonon scattering coefficients within density functional theory. The three phonons can have three arbitrary wave vectors $(\mathbf{q},\mathbf{q}',\mathbf{q}'')$. The approach works for materials with an electronic gap and also for metallic or zero gap materials. The method has been implemented in the QUANTUM ESPRESSO package[11] and generalizes a previously existing code developed in Ref. 14. The anharmonic coefficients, which can be obtained, can be used in a straightforward way to compute the anharmonic broadening of a phonon with an arbitrary wave vector $\mathbf{q}$ and the intrinsic thermal conductivity within the single-mode relaxation time approximation (SMA). The first applications have been devoted to study graphite, graphene, and mono- and bilayers.

We have reported a detailed analysis of the anharmonic phonon broadening in graphene. Interestingly, the broadening of the high-energy optical branches is highly nonuniform and presents a series of sudden steps and spikes of various origin. At finite temperature, the two linearly dispersive acoustic branches TA and LA have nonzero broadening for $q \to 0$, as noticed in Ref. 9. This anomalous behavior is due to normal scattering towards two ZA phonons (which are quadratically dispersive), for small q. The activation of the umklapp scattering for sufficiently large q is associated with a sudden increase of the broadening at nearly half the Wigner Seitz cell. We provide a set of expressions, which can be used to fit the anharmonic scattering time and broadening for the acoustic phonon branches, which are the most relevant in thermal transport.

The broadening of graphite and bilayer is, overall, very similar to the graphene one. The most remarkable feature is the

broadening of the quasiacoustical ZO′ branch, which is much larger and very different from the one of the strictly related ZA acoustic branch. On the other hand, the broadening of the TA and LA branches of graphite, displays a certain number of similarities with that of graphene mono- and bilayers, in spite of the different dimensionality of the systems.

Finally, we have calculated the intrinsic anharmonic thermal conductivity within the SMA. The in-plane conductivities in graphite, graphene, and mono- and bilayers are very similar in spite of the differences among these systems. The calculated SMA conductivity heavily underestimates the measured one (for graphite) by almost a factor two, in the temperature range from 200 to 2000 K. This finding is compatible with the conclusions of Refs. 27 and 30, which state that the SMA cannot be used to properly describe the in-plane thermal conductivity in graphitic materials. On the other hand, the calculated SMA conductivity for graphite along the direction perpendicular to the plane is in good agreement with measurements.

ACKNOWLEDGMENTS

This work was financed by ANR project ACCATTONE. Calculations were done at IDRIS (Orsay, France), Project No. 096128 and CINES Project *imp6128*. We thank G. Fugallo for discussions.

APPENDIX A: THIRD-ORDER CALCULATION

This section describes the method used to calculate the third-order anharmonic scattering coefficients. In order to fix the notation, Secs. A 1 and A 2 resume DFT and linear response to DFT (alias DFPT). Third-order calculations are described in Sec. A 3. Sections A 4 and A 5 give the explicit expressions for certain terms. Section A 6 describes the implementation of the nonlinear core corrections.

1. Kohn-Sham equations

Within DFT, the total energy of a system can be determined from the ground-state electronic charge density n. In turn, n can be obtained by solving self-consistently the Kohn Sham (KS) equations,[31] which, in a periodic crystal are

$$(T^{\rm kin} + V^{\rm KS})|\psi_{\mathbf{k},i}\rangle = \epsilon_{\mathbf{k},i}|\psi_{\mathbf{k},i}\rangle, \tag{A1}$$

$$V^{\rm KS}(\mathbf{r}) = v^{\rm ion}(\mathbf{r}) + \frac{\delta E_{\rm I}[n]}{\delta n(\mathbf{r})}, \tag{A2}$$

$$n(\mathbf{r}) = \sum_{\mathbf{k},i} \tilde{\theta}_{\mathbf{k},i}|\langle\psi_{\mathbf{k},i}|\mathbf{r}\rangle|^2; \quad \int n(\mathbf{r})d\mathbf{r} = N^{\rm el}. \tag{A3}$$

In Eq. (A1), $T^{\rm kin}$ is the single-particle kinetic energy operator, $V^{\rm KS}$ is the KS potential, $|\psi_{\mathbf{k},i}\rangle$ are the Bloch eigenstates with wave vector $\mathbf{k}$, band index i, and energy $\epsilon_{\mathbf{k},i}$. $\langle\mathbf{r}+\mathbf{R}|\psi_{\mathbf{k},i}\rangle = e^{i\mathbf{k}\cdot\mathbf{R}}\langle\mathbf{r}|\psi_{\mathbf{k},i}\rangle$, being $\mathbf{r}$ the position and $\mathbf{R}$ a lattice vector. $v^{\rm ion}$ is the external potential due to the ions, $E_{\rm I}[n]$ is the interaction functional (Hartree energy plus exchange-correlation contribution). The sum in Eq. (A3) is done on a sufficiently fine grid of $\mathbf{k}$ points. $\tilde{\theta}_{\mathbf{k},i}$ is the occupation of an electronic state: $\tilde{\theta}_{\mathbf{k},i} = 1$ for valence band electrons and $\tilde{\theta}_{\mathbf{k},i} = 0$ for conduction ones. Here and in the following, $\int d\mathbf{r}$ is the integral over all the space. $N^{\rm el}$ is the total number of valence electrons (we consider $e^2 = 1$). The total energy of the system is

$$\mathcal{E}^{\rm tot} = E^{\rm ion} + \sum_{\mathbf{k},i}\epsilon_{\mathbf{k},i}\tilde{\theta}_{\mathbf{k},i} + E_{\rm I}[n] - \int \frac{\delta E_{\rm I}[n]}{\delta n(\mathbf{r})}n(\mathbf{r})d\mathbf{r}, \tag{A4}$$

where $E^{\rm ion}$ is the ionic contribution.

In this form, the KS equations are suitable for semiconductor or insulators, where the electronic gap is different from zero. If the electronic gap vanishes (metal and semimetal cases), it is customary[32] to introduce a smearing function $\theta_\sigma(x)$, which is characterized by a smearing width σ and which becomes a step function in the limit $\sigma \to 0$. The KS equation are still written as in Eqs. (A1)–(A3) but now $\tilde{\theta}_{\mathbf{k},i} = \theta_\sigma(\epsilon_{\rm F} - \epsilon_{\mathbf{k},i})$, where the Fermi energy $\epsilon_{\rm F}$ has to be determined self-consistently from

$$\sum_{\mathbf{k},i}\tilde{\theta}_{\mathbf{k},i} = N^{\rm el}. \tag{A5}$$

Furthermore, in the metallic case, a proper definition of the energy $\mathcal{E}^{\rm tot}$ requires[33] Eq. (A4) to include the term

$$\sum_{\mathbf{k},i}\int_{-\infty}^{\epsilon_{\rm F}-\epsilon_{\mathbf{k},i}} x\delta_\sigma(x)dx, \tag{A6}$$

where $\delta_\sigma(x) = \partial\theta_\sigma(x)/(\partial x)$.

2. Linear response

The derivative of the electronic charge distribution with respect to the $\mathbf{q}$ periodic displacement $u_{\mathbf{q}}$, as defined in Eq. (1) (for simplicity, from now on we will drop the indexes α and s), can be obtained from the first-order perturbation theory.[10] For the metallic case, linear response can be implemented following Ref. 33; we will follow the equivalent, but slightly different approach of Ref. 14.

Let us consider a uniform grid of electronic $\mathbf{k}$ points and a phonon wave vector $\mathbf{q}$, which belongs to this grid. First, one has to solve the KS equations and obtain the ground-state change density n and the corresponding KS wave functions $|\psi_{\mathbf{k},i}\rangle$. Then, one has to define a "cutoff" energy $\overline{E}$, which separates the electronic states that are completely empty from those which are occupied or partially occupied. In the semiconductor/insulator case, $\overline{E}$ can be any energy within the gap; in the metallic case, any $\overline{E} \geqslant \epsilon_{\rm F} + 3\sigma$ is a reasonable choice. We define P_c as the projector on the manifold spanned by the empty states and $P_v = 1 - P_c$ as the projector onto the occupied and partially occupied states.

The derivative of the charge $\partial n/\partial u_{\mathbf{q}}$ and the derivative of the KS wave functions projected onto the conduction bands $|\phi^{\mathbf{q}}_{\mathbf{k},i}\rangle = P_c|\partial\psi_{\mathbf{k},i}/\partial u_{\mathbf{q}}\rangle$ can be obtained by solving self-consistently the equations

$$(T^{\rm kin} + V^{\rm KS} + \alpha P_v - \epsilon_{\mathbf{k},i})\big|\phi^{\mathbf{q}}_{\mathbf{k}i}\big\rangle = -P_c\frac{\partial V_{\rm KS}}{\partial u_{\mathbf{q}}}|\psi_{\mathbf{k}i}\rangle, \tag{A7}$$

$$\frac{\partial V^{\rm KS}(\mathbf{r})}{\partial u_{\mathbf{q}}} = \frac{\partial v^{\rm ion}(\mathbf{r})}{\partial u_{\mathbf{q}}} + \int \frac{\delta^2 E_{\rm I}[n]}{\delta n(\mathbf{r})\delta n(\mathbf{r}')}\frac{\partial n(\mathbf{r}')}{\partial u_{\mathbf{q}}}d\mathbf{r}', \tag{A8}$$

$$\frac{\partial n(\mathbf{r})}{\partial u_{\mathbf{q}}} = \sum_{\mathbf{k}} \langle \mathbf{r}| \Bigg[\sum_i \tilde{\delta}_{\mathbf{k}i} \epsilon_{\mathrm{F}}^{\mathbf{q}} |\psi_{\mathbf{k}i}\rangle\langle\psi_{\mathbf{k}i}| + \sum_{i,j}^{v} \frac{\tilde{\theta}_{\mathbf{k}i} - \tilde{\theta}_{\mathbf{k}+\mathbf{q},j}}{\epsilon_{\mathbf{k}i} - \epsilon_{\mathbf{k}+\mathbf{q},j}} |\psi_{\mathbf{k}+\mathbf{q},j}\rangle\langle\psi_{\mathbf{k}+\mathbf{q},j}| V^{\mathbf{q}} |\psi_{\mathbf{k}i}\rangle\langle\psi_{\mathbf{k}i}| + \sum_i \tilde{\theta}_{\mathbf{k}i} \left(|\phi_{\mathbf{k}i}^{\mathbf{q}}\rangle\langle\psi_{\mathbf{k}i}| + |\psi_{\mathbf{k}i}\rangle\langle\phi_{\mathbf{k}i}^{-\mathbf{q}}| \right) \Bigg] |\mathbf{r}\rangle. \tag{A9}$$

α is a constant chosen in such a way that the linear system of Eq. (A7) is not singular, $\sum^{v}$ indicates that the sum is to be performed only on the partially occupied states, and $\tilde{\delta}_{\mathbf{k},i} = \delta_\sigma(\epsilon_{\mathrm{F}} - \epsilon_{\mathbf{k},i})$.

The first two terms in the right-hand side of Eq. (A9) are different from zero only in the metallic case and are written using the notation $\epsilon_{\mathrm{F}}^{\mathbf{q}} = \partial\epsilon_{\mathrm{F}}/\partial u_{\mathbf{q}}$ and $V^{\mathbf{q}} = \partial V_{\mathrm{KS}}/\partial u_{\mathbf{q}}$. $\epsilon_{\mathrm{F}}^{\mathbf{q}} = 0$ for $\mathbf{q} \neq \mathbf{0}$; it has to be determined self-consistently from

$$\epsilon_{\mathrm{F}}^{\mathbf{q}} = \frac{\sum_{\mathbf{k},i} \langle \psi_{\mathbf{k},i} | V^{\mathbf{q}} | \psi_{\mathbf{k},i} \rangle}{\sum_{\mathbf{k},i} \tilde{\delta}_{\mathbf{k},i}}. \tag{A10}$$

In the second line of Eq. (A9), we have used a compact notation which reads: when the denominator is equal to zero, one has to substitute the ratio with its limit as the denominator approaches zero. The same substitution can be used when the denominator is very small in order to gain numerical stability. Thus, when $\epsilon_{\mathbf{k}i} \sim \epsilon_{\mathbf{k}+\mathbf{q},j}$, one can substitute $(\tilde{\theta}_{\mathbf{k}i} - \tilde{\theta}_{\mathbf{k}+\mathbf{q},j})/(\epsilon_{\mathbf{k}i} - \epsilon_{\mathbf{k}+\mathbf{q},j})$ with $-\tilde{\delta}_{\mathbf{k},i}$. We finally note that the present approach is different from the one described in Ref. 33 and that the $|\phi\rangle$ wave functions presently defined (which are the same as in Ref. 14) are different from the $|\phi\rangle$ of Ref. 33.

3. Third order

Let us consider three phonon displacements $u_{\mathbf{q}}$, $u_{\mathbf{q}'}$, $u_{\mathbf{q}''}$ such that the sum of their wave vectors is $\mathbf{q} + \mathbf{q}' + \mathbf{q}'' = \mathbf{0}$. By solving the linear response equations, one can obtain $\partial n/\partial u_{\mathbf{q}}$ and the $\{|\phi_{\mathbf{k},i}^{\mathbf{q}}\rangle\}$ corresponding to the three phonons. The third derivative of the energy can then be obtained from

$$\frac{\partial^3 \mathcal{E}^{\mathrm{tot}}}{\partial u_{\mathbf{q}} \partial u_{\mathbf{q}'} \partial u_{\mathbf{q}''}} = \tfrac{1}{6} (\tilde{E}^{\mathbf{q},\mathbf{q}',\mathbf{q}''} + \tilde{E}^{\mathbf{q}'',\mathbf{q},\mathbf{q}'} + \tilde{E}^{\mathbf{q}',\mathbf{q}'',\mathbf{q}} + \tilde{E}^{\mathbf{q},\mathbf{q}'',\mathbf{q}'} + \tilde{E}^{\mathbf{q}'',\mathbf{q}',\mathbf{q}} + \tilde{E}^{\mathbf{q}',\mathbf{q},\mathbf{q}''}), \tag{A11}$$

$$\tilde{E}^{\mathbf{q},\mathbf{q}',\mathbf{q}''} = Z^{\mathbf{q},\mathbf{q}',\mathbf{q}''} + \frac{\partial^3 E^{\mathrm{ion}}}{\partial u_{\mathbf{q}} \partial u_{\mathbf{q}'} \partial u_{\mathbf{q}''}} + \int n(\mathbf{r}) \frac{\partial^3 v^{\mathrm{ion}}(\mathbf{r})}{\partial u_{\mathbf{q}} \partial u_{\mathbf{q}'} \partial u_{\mathbf{q}''}} d\mathbf{r} + 3 \int \frac{\partial n(\mathbf{r})}{\partial u_{\mathbf{q}}} \frac{\partial^2 v^{\mathrm{ion}}(\mathbf{r})}{\partial u_{\mathbf{q}'} \partial u_{\mathbf{q}''}} d\mathbf{r} + \iiint \frac{\delta^3 E_{\mathrm{I}}[n]}{\delta n(\mathbf{r}) \delta n(\mathbf{r}') \delta n(\mathbf{r}'')} \frac{\partial n(\mathbf{r})}{\partial u_{\mathbf{q}}} \frac{\partial n(\mathbf{r}')}{\partial u_{\mathbf{q}'}} \frac{\partial n(\mathbf{r}'')}{\partial u_{\mathbf{q}''}} d\mathbf{r} d\mathbf{r}' d\mathbf{r}''. \tag{A12}$$

For the semiconductor/insulator case, we can follow Ref. 13 and write

$$Z^{\mathbf{q},\mathbf{q}',\mathbf{q}''} = 6 \sum_{\mathbf{k}} \left(\sum_i \tilde{\theta}_{\mathbf{k}i} \langle \phi_{\mathbf{k}i}^{-\mathbf{q}} | V^{\mathbf{q}'} | \phi_{\mathbf{k}i}^{\mathbf{q}''} \rangle - \sum_{i,j}^{v} \tilde{\theta}_{\mathbf{k}i} \langle \phi_{\mathbf{k}+\mathbf{q},i}^{-\mathbf{q}} | \phi_{\mathbf{k}-\mathbf{q}',j}^{\mathbf{q}'} \rangle \langle \psi_{\mathbf{k}-\mathbf{q}',j} | V^{\mathbf{q}''} | \psi_{\mathbf{k}+\mathbf{q},i} \rangle \right). \tag{A13}$$

For the metallic case, we follow Ref. 14:

$$\begin{aligned} Z^{\mathbf{q},\mathbf{q}',\mathbf{q}''} = \sum_{\mathbf{k}} \Bigg\{ & 6 \sum_i \tilde{\theta}_{\mathbf{k}i} \langle \phi_{\mathbf{k}i}^{-\mathbf{q}} | V^{\mathbf{q}'} | \phi_{\mathbf{k}i}^{\mathbf{q}''} \rangle + 6 \sum_{i,j}^{v} \frac{\left(\tilde{\theta}_{\mathbf{k}+\mathbf{q},i} \langle \phi_{\mathbf{k}+\mathbf{q},i}^{-\mathbf{q}} | V^{\mathbf{q}'} | \psi_{\mathbf{k}-\mathbf{q}',j} \rangle - \tilde{\theta}_{\mathbf{k}-\mathbf{q}',j} \langle \psi_{\mathbf{k}+\mathbf{q},i} | V^{\mathbf{q}} | \phi_{\mathbf{k}-\mathbf{q}',j}^{\mathbf{q}'} \rangle \right) \langle \psi_{\mathbf{k}-\mathbf{q}',j} | V^{\mathbf{q}''} | \psi_{\mathbf{k}+\mathbf{q},i} \rangle}{\epsilon_{\mathbf{k}+\mathbf{q},i} - \epsilon_{\mathbf{k}-\mathbf{q}',j}} \\ & + 2 \sum_{i,j,l}^{v} \Bigg[\langle \psi_{\mathbf{k},i} | V^{\mathbf{q}} | \psi_{\mathbf{k}-\mathbf{q},j} \rangle \langle \psi_{\mathbf{k}-\mathbf{q},j} | V^{\mathbf{q}'} | \psi_{\mathbf{k}+\mathbf{q}'',l} \rangle \langle \psi_{\mathbf{k}+\mathbf{q}'',l} | V^{\mathbf{q}''} | \psi_{\mathbf{k},i} \rangle \\ & \times \frac{\tilde{\theta}_{\mathbf{k},i}(\epsilon_{\mathbf{k}-\mathbf{q},j} - \epsilon_{\mathbf{k}+\mathbf{q}'',l}) + \tilde{\theta}_{\mathbf{k}-\mathbf{q},j}(\epsilon_{\mathbf{k}+\mathbf{q}'',l} - \epsilon_{\mathbf{k},i}) + \tilde{\theta}_{\mathbf{k}+\mathbf{q}'',l}(\epsilon_{\mathbf{k},i} - \epsilon_{\mathbf{k}-\mathbf{q},j})}{(\epsilon_{\mathbf{k},i} - \epsilon_{\mathbf{k}-\mathbf{q},j})(\epsilon_{\mathbf{k}-\mathbf{q},j} - \epsilon_{\mathbf{k}+\mathbf{q}'',l})(\epsilon_{\mathbf{k}+\mathbf{q}'',l} - \epsilon_{\mathbf{k},i})} \Bigg] \\ & + 3\epsilon_{\mathrm{F}}^{\mathbf{q}} \left(\sum_{i,j}^{v} \frac{\tilde{\delta}_{\mathbf{k},i} - \tilde{\delta}_{\mathbf{k}+\mathbf{q}'',j}}{\epsilon_{\mathbf{k},i} - \epsilon_{\mathbf{k}+\mathbf{q}'',j}} \langle \psi_{\mathbf{k},i} | V^{\mathbf{q}'} | \psi_{\mathbf{k}+\mathbf{q}'',j} \rangle \langle \psi_{\mathbf{k}+\mathbf{q}'',j} | V^{\mathbf{q}''} | \psi_{\mathbf{k},i} \rangle + 2 \sum_i \tilde{\delta}_{\mathbf{k},i} \langle \psi_{\mathbf{k},i} | V^{\mathbf{q}'} | \phi_{\mathbf{k},j}^{\mathbf{q}''} \rangle \right) \\ & + 3\epsilon_{\mathrm{F}}^{\mathbf{q}} \epsilon_{\mathrm{F}}^{\mathbf{q}'} \left(\sum_i \tilde{\delta}_{\mathbf{k},i}^{(1)} \langle \psi_{\mathbf{k},i} | V^{\mathbf{q}''} | \psi_{\mathbf{k},i} \rangle \right) - \epsilon_{\mathrm{F}}^{\mathbf{q}} \epsilon_{\mathrm{F}}^{\mathbf{q}'} \epsilon_{\mathrm{F}}^{\mathbf{q}''} \left(\sum_i \tilde{\delta}_{\mathbf{k},i}^{(1)} \right) \Bigg\}, \end{aligned} \tag{A14}$$

where $\tilde{\delta}_{\mathbf{k},i}^{(1)} = \partial\delta_\sigma(x)/(\partial x)|_{x=\epsilon_{\mathrm{F}}-\epsilon_{\mathbf{k},i}}$. Equation (A14) is written with the same compact notation of Eq. (A9): when one of the denominators in Eq. (A14) vanishes, the corresponding term is replaced with its limit. In particular, when $\epsilon_{\mathbf{k}+\mathbf{q},i} \sim \epsilon_{\mathbf{k}-\mathbf{q}',j}$ in the second line of Eq. (A14), the argument of the sum can be written as

$$-\left(\tilde{\theta}_{\mathbf{k}+\mathbf{q},i} \langle \phi_{\mathbf{k}+\mathbf{q},i}^{-\mathbf{q}} | \phi_{\mathbf{k}-\mathbf{q}',j}^{\mathbf{q}'} \rangle + \tilde{\delta}_{\mathbf{k}+\mathbf{q},i} \langle \psi_{\mathbf{k}+\mathbf{q},i} | V^{\mathbf{q}} | \phi_{\mathbf{k}-\mathbf{q}',j}^{\mathbf{q}'} \rangle \right) \langle \psi_{\mathbf{k}-\mathbf{q}',j} | V^{\mathbf{q}''} | \psi_{\mathbf{k}+\mathbf{q},i} \rangle.$$

The limits of the factor in the fourth line of Eq. (A14) are

$$\begin{aligned}
&\text{for}\quad \epsilon_{\mathbf{k},i} \sim \epsilon_{\mathbf{k}-\mathbf{q},j} \neq \epsilon_{\mathbf{k}+\mathbf{q}'',l} : \left(\frac{\tilde{\theta}_{\mathbf{k},i} - \tilde{\theta}_{\mathbf{k}+\mathbf{q}'',l}}{\epsilon_{\mathbf{k},i} - \epsilon_{\mathbf{k}+\mathbf{q}'',l}} + \tilde{\delta}_{\mathbf{k},i}\right) \frac{1}{\epsilon_{\mathbf{k}+\mathbf{q}'',l} - \epsilon_{\mathbf{k},i}},\\
&\text{for}\quad \epsilon_{\mathbf{k}-\mathbf{q},j} \sim \epsilon_{\mathbf{k}+\mathbf{q}'',l} \neq \epsilon_{\mathbf{k},i} : \left(\frac{\tilde{\theta}_{\mathbf{k}-\mathbf{q},j} - \tilde{\theta}_{\mathbf{k},i}}{\epsilon_{\mathbf{k}-\mathbf{q},j} - \epsilon_{\mathbf{k},i}} + \tilde{\delta}_{\mathbf{k}-\mathbf{q},j}\right) \frac{1}{\epsilon_{\mathbf{k},i} - \epsilon_{\mathbf{k}-\mathbf{q},j}},\\
&\text{for}\quad \epsilon_{\mathbf{k}+\mathbf{q}'',l} \sim \epsilon_{\mathbf{k},i} \neq \epsilon_{\mathbf{k}-\mathbf{q},j} : \left(\frac{\tilde{\theta}_{\mathbf{k}+\mathbf{q}'',l} - \tilde{\theta}_{\mathbf{k}-\mathbf{q},j}}{\epsilon_{\mathbf{k}+\mathbf{q}'',l} - \epsilon_{\mathbf{k}-\mathbf{q},j}} + \tilde{\delta}_{\mathbf{k}+\mathbf{q}'',l}\right) \frac{1}{\epsilon_{\mathbf{k}-\mathbf{q},j} - \epsilon_{\mathbf{k}+\mathbf{q}'',l}},\quad \text{for}\quad \epsilon_{\mathbf{k},i} \sim \epsilon_{\mathbf{k}-\mathbf{q},j} \sim \epsilon_{\mathbf{k}+\mathbf{q}'',l} : -\frac{1}{2}\tilde{\delta}^{(1)}_{\mathbf{k},i}.
\end{aligned} \tag{A15}$$

Finally, in the fifth line of Eq. (A14), when $\epsilon_{\mathbf{k}i} \sim \epsilon_{\mathbf{k}+\mathbf{q}'',j}$ one can substitute $(\tilde{\delta}_{\mathbf{k}i} - \tilde{\delta}_{\mathbf{k}+\mathbf{q}'',j})/(\epsilon_{\mathbf{k}i} - \epsilon_{\mathbf{k}+\mathbf{q}'',j})$ with $-\tilde{\delta}^{(1)}_{\mathbf{k},i}$.

Once the derivative in Eq. (A11) has been determined, one can obtain the phonon scattering coefficients by combining Eqs. (4) and (5). Provided that $\mathbf{G}$ is vector of the reciprocal lattice, we also remark that

$$\frac{\partial^3 \mathcal{E}^{\text{tot}}}{\partial u_{\mathbf{q}} \partial u_{\mathbf{q}'} \partial u_{\mathbf{q}''+\mathbf{G}}} = \frac{\partial^3 \mathcal{E}^{\text{tot}}}{\partial u_{\mathbf{q}} \partial u_{\mathbf{q}'} \partial u_{\mathbf{q}''}}. \tag{A16}$$

Hence we have not lost generality by imposing $\mathbf{q} + \mathbf{q}' + \mathbf{q}'' = \mathbf{0}$ at the beginning of the present section.

Given a computer code that implements linear response to DFT (DFPT), all the bra-ket products described in this section can be obtained straightforwardly. On the other hand, the computation of the second to the fourth terms in the right-hand side of Eq. (A12) have to be implemented from scratch. The implementation of the fourth term is trivial within the local density approximation. The expressions required for the other terms are given below.

4. Ionic contribution

The second term in the right-hand side of Eq. (A12) is the third derivative of the ion-ion contribution to the total energy. It is computed, as customary, using the Ewald sum technique:[34]

$$\begin{aligned}
\frac{\partial^3 E^{\text{ion}}}{\partial u_{\mathbf{q},s,\alpha} \partial u_{\mathbf{q}',s',\beta} \partial u_{\mathbf{q}'',s'',\gamma}} &= \delta_{s',s''} Z_{s'} Z_s F_{\alpha,\beta,\gamma}(\mathbf{q}, \mathbf{t}_{s'} - \mathbf{t}_s)\\
&+ \delta_{s'',s} Z_{s''} Z_{s'} F_{\alpha,\beta,\gamma}(\mathbf{q}', \mathbf{t}_{s''} - \mathbf{t}_{s'})\\
&+ \delta_{s,s'} Z_s Z_{s''} F_{\alpha,\beta,\gamma}(\mathbf{q}'', \mathbf{t}_s - \mathbf{t}_{s''})\\
&- \delta_{s,s',s''} Z_s \sum_{\tilde{s}} Z_{\tilde{s}} F_{\alpha,\beta,\gamma}(\mathbf{0}, \mathbf{t}_s - \mathbf{t}_{\tilde{s}}).
\end{aligned} \tag{A17}$$

In Eq. (A17), we have written explicitly the dependence on the atomic (s,s',s'') and Cartesian (α,β,γ) indexes of the phonon patterns $u_{\mathbf{q}}$ [defined in Eq. (1)]. In Eq. (A17), Z_s is the ionic charge and $\mathbf{t}_s$ is the position of atom s. The sum is performed over all the atoms of the unit cell. The function F is

$$\begin{aligned}
F_{\alpha,\beta,\gamma}(\mathbf{q},\mathbf{t}) = -\frac{4\pi}{\Omega} \sum_{\mathbf{G}} \Bigg[&\frac{e^{-(\mathbf{G}+\mathbf{q})^2/(4\eta^2)}}{(\mathbf{G}+\mathbf{q})^2} e^{i(\mathbf{G}+\mathbf{q})\cdot\mathbf{t}}\\
&\times i^3 (\mathbf{G}+\mathbf{q})_\alpha (\mathbf{G}+\mathbf{q})_\beta (\mathbf{G}+\mathbf{q})_\gamma \Bigg]\\
- \sum_{\mathbf{R}} e^{i\mathbf{q}\cdot\mathbf{R}} &\left.\frac{d^3 f(\mathbf{x})}{dx_\alpha dx_\beta dx_\gamma}\right|_{\mathbf{x}=\mathbf{t}-\mathbf{R}}.
\end{aligned} \tag{A18}$$

Here, Ω is the unit-cell volume, the sums are performed on the ensemble of the reciprocal lattice vectors $\mathbf{G}$ and of the real space lattice vectors $\mathbf{R}$. η is the cutoff for the real space summation within the Ewald method[34] and $f(\mathbf{x}) = \text{erfc}(\eta|\mathbf{x}|)/|\mathbf{x}|$, where erfc is the error function. The derivative of f is

$$\begin{aligned}
\frac{d^3 f(\mathbf{x})}{dx_\alpha dx_\beta dx_\gamma} &= (\delta_{\alpha\beta} x_\gamma + \delta_{\beta\gamma} x_\alpha + \delta_{\gamma\alpha} x_\beta) f_1(|\mathbf{x}|)\\
&+ x_\alpha x_\beta x_\gamma f_2(|\mathbf{x}|)
\end{aligned} \tag{A19}$$

with

$$\begin{aligned}
f_1(x) &= \frac{3\text{erfc}(\eta x) + a(\eta x)(3 + 2\eta^2 x^2)}{x^5},\\
f_2(x) &= -\frac{15\text{erfc}(\eta x) + a(\eta x)(15 + 10\eta^2 x^2 + 4\eta^4 x^4)}{x^7},\\
a(\xi) &= \frac{2\xi}{\sqrt{\pi}} e^{-\xi^2}.
\end{aligned}$$

5. Derivatives of the external potential

Here, we give the expressions to calculate the third and fourth terms in the right-hand side of Eq. (A12). Both terms are convenient to evaluate in the reciprocal space. v^{ion} in Eq. (A12) corresponds to the electrostatic potential induced by the atomic ions. Within the present approach, an atom s acts through a pseudopotential, which, within the Kleinman-Bylander scheme,[35] is nonlocal and can be written as

$$v_s(\mathbf{r},\mathbf{r}') = v_s^{\text{loc}}(\mathbf{r}) \delta(\mathbf{r} - \mathbf{r}') + \sum_{\mu,\nu} D^s_{\mu,\nu} P_{\mu,s}(\mathbf{r}) P_{\nu,s}(\mathbf{r}'), \tag{A20}$$

where v_s^{loc} is the local component of the potential; $D^s_{\mu,\nu} = D^s_{\nu,\mu}$ are coefficients and $P_{\mu,s}$ are ion-centered projectors. The total ionic potential is a superposition of ionic potentials:

$$v^{\text{ion}}(\mathbf{r},\mathbf{r}') = \sum_{\mathbf{R},s} v_s(\mathbf{r} - \mathbf{t}_s - \mathbf{R}, \mathbf{r}' - \mathbf{t}_s - \mathbf{R}), \tag{A21}$$

where the sum is performed on all the lattice vectors $\mathbf{R}$ and on the atoms s in the unit cell. When v^{ion} is local, its trace with the charge density is $\int v^{\text{ion}}(\mathbf{r}) n(\mathbf{r}) d\mathbf{r}$. When v^{ion} is nonlocal, the same quantity is $\sum_{\mathbf{k},i} \tilde{\theta}_{\mathbf{k},i} \int d\mathbf{r} \int d\mathbf{r}' \psi^*_{\mathbf{k},i}(\mathbf{r}) v^{\text{ion}}(\mathbf{r},\mathbf{r}') \psi^*_{\mathbf{k},i}(\mathbf{r}')$.

With this notation,

$$\int n(\mathbf{r})v^{\mathrm{ion}}(\mathbf{r})d\mathbf{r} = \frac{1}{\Omega}\sum_{\mathbf{G},s} n(-\mathbf{G})v_s^{\mathrm{loc}}(\mathbf{G})e^{-i\mathbf{G}\cdot\mathbf{t}_s} + \frac{1}{N}\sum_{\substack{\mathbf{k},i\\ \mu,\nu,s}} D^s_{\mu,\nu}\tilde{\theta}_{\mathbf{k},i}A_{\substack{\mathbf{k},i\\ \mu,s}}\left(A_{\substack{\mathbf{k},i\\ \nu,s}}\right)^*, \quad \text{(A22)}$$

$$A_{\substack{\mathbf{k},i\\ \mu,s}} = \frac{1}{\Omega}\sum_{\mathbf{G}} \psi^*_{\mathbf{k},i}(\mathbf{G})P_{\mu,s}(\mathbf{k}+\mathbf{G})e^{-i\mathbf{G}\cdot\mathbf{t}_s}. \quad \text{(A23)}$$

Here, $n(\mathbf{k})$, $v_s^{\mathrm{loc}}(\mathbf{k})$, and $P_{\mu,s}(\mathbf{k})$ are the Fourier transforms of $n(\mathbf{r})$, $v_s^{\mathrm{loc}}(\mathbf{r})$, and $P_{\mu,s}(\mathbf{r})$. The Fourier transform of $f(\mathbf{r})$ is defined as $f(\mathbf{k}) = \int e^{-i\mathbf{k}\cdot\mathbf{r}}f(\mathbf{r})d\mathbf{r}$, where the integral is done all over the space. Given a Bloch wave function $\psi_{\mathbf{k},i}(\mathbf{r})$, we define $\psi_{\mathbf{k},i}(\mathbf{G}) = \int e^{-i(\mathbf{k}+\mathbf{G})\cdot\mathbf{r}}\psi_{\mathbf{k},i}(\mathbf{r})d\mathbf{r}$, that is, $\psi_{\mathbf{k},i}(\mathbf{r}) = 1/(N\Omega)\sum_{\mathbf{G}} e^{i(\mathbf{k}+\mathbf{G})\cdot\mathbf{r}}\psi_{\mathbf{k},i}(\mathbf{G})$.

To simplify the notation, we notice that the derivative of the charge, Eq. (A9), can be rewritten as

$$\frac{\partial n}{\partial u_{\mathbf{q}}}(\mathbf{r}) = \sum_{\mathbf{k},i}\tilde{\theta}_{\mathbf{k},i}\left\{\tilde{\phi}^{\mathbf{q}}_{\mathbf{k},i}(\mathbf{r})\psi^*_{\mathbf{k},i}(\mathbf{r}) + \psi_{\mathbf{k},i}(\mathbf{r})\left[\tilde{\phi}^{-\mathbf{q}}_{\mathbf{k},i}(\mathbf{r})\right]^*\right\},$$

and we define

$$\tilde{\phi}^{\mathbf{q}}_{\mathbf{k},i}(\mathbf{G}) = \int e^{-i(\mathbf{k}+\mathbf{q}+\mathbf{G})\cdot\mathbf{r}}\tilde{\phi}^{\mathbf{q}}_{\mathbf{k},i}(\mathbf{r})d\mathbf{r}.$$

By using the above definitions, the third and the fourth terms in the right-hand side of Eq. (A12) are

$$\int n(\mathbf{r})\frac{\partial^3 v^{\mathrm{ion}}(\mathbf{r})}{\partial u_{\mathbf{q},s,\alpha}\partial u_{\mathbf{q}',s',\beta}\partial u_{\mathbf{q}'',s'',\gamma}}d\mathbf{r} = \frac{\delta_{s,s',s''}}{\Omega}\sum_{\mathbf{G}} n(-\mathbf{G})(-i)^3 G_\alpha G_\beta G_\gamma v_s^{\mathrm{loc}}(\mathbf{G})e^{-i\mathbf{G}\cdot\mathbf{t}_s} + \frac{\delta_{s,s',s''}}{N}\sum_{\substack{\mathbf{k},i\\ \mu,\nu}} D^s_{\mu,\nu}\tilde{\theta}_{\mathbf{k},i}$$
$$\times\left\{A^{(\alpha,\beta,\gamma)}_{\substack{\mathbf{k},i\\ \mu,s}}\left(A_{\substack{\mathbf{k},i\\ \nu,s}}\right)^* + \overline{A^{(\alpha,\beta)}_{\substack{\mathbf{k},i\\ \mu,s}}\left[A^{(\gamma)}_{\substack{\mathbf{k},i\\ \nu,s}}\right]^*} + \overline{A^{(\alpha)}_{\substack{\mathbf{k},i\\ \mu,s}}\left[A^{(\beta,\gamma)}_{\substack{\mathbf{k},i\\ \nu,s}}\right]^*} + A_{\substack{\mathbf{k},i\\ \mu,s}}\left[A^{(\alpha,\beta,\gamma)}_{\substack{\mathbf{k},i\\ \nu,s}}\right]^*\right\}, \quad \text{(A24)}$$

$$\int \frac{\partial n(\mathbf{r})}{\partial u_{\mathbf{q},s,\alpha}}\frac{\partial^2 v^{\mathrm{ion}}(\mathbf{r})}{\partial u_{\mathbf{q}',s',\beta}\partial u_{\mathbf{q}'',s'',\gamma}}d\mathbf{r} = \frac{\delta_{s',s''}}{\Omega}\sum_{\mathbf{G}}\frac{\partial n(-\mathbf{G})}{\partial u_{-\mathbf{q},s,\alpha}}(-i)^2(\mathbf{q}+\mathbf{G})_\beta(\mathbf{q}+\mathbf{G})_\gamma v_{s'}^{\mathrm{loc}}(\mathbf{q}+\mathbf{G})e^{-i(\mathbf{q}+\mathbf{G})\cdot\mathbf{t}_{s'}} + 2\frac{\delta_{s',s''}}{N}\sum_{\substack{\mathbf{k},i\\ \mu,\nu}}$$
$$\times D^{s'}_{\mu,\nu}\tilde{\theta}_{\mathbf{k},i}\left\{A^{(\beta,\gamma)}_{\substack{\mathbf{k},i\\ \mu,s'}}\left(B_{\substack{\mathbf{q},\mathbf{k},i\\ \nu,s'}}\right)^* + A^{(\beta)}_{\substack{\mathbf{k},i\\ \mu,s'}}\left[B^{(\gamma)}_{\substack{\mathbf{q},\mathbf{k},i\\ \nu,s'}}\right]^* + A^{(\gamma)}_{\substack{\mathbf{k},i\\ \mu,s'}}\left[B^{(\beta)}_{\substack{\mathbf{q},\mathbf{k},i\\ \nu,s'}}\right]^* + A_{\substack{\mathbf{k},i\\ \mu,s'}}\left[B^{(\beta,\gamma)}_{\substack{\mathbf{q},\mathbf{k},i\\ \nu,s'}}\right]^*\right\}. \quad \text{(A25)}$$

In Eq. (A24), the overline indicates the sum on the permutations of the Cartesian indexes, e.g., $\overline{A^{\alpha\beta}(A^\gamma)^*} = A^{\alpha\beta}(A^\gamma)^* + A^{\beta\gamma}(A^\alpha)^* + A^{\gamma\alpha}(A^\beta)^*$. Furthermore, $\frac{\partial n(\mathbf{G})}{\partial u_{\mathbf{q}}}$ is the Fourier transform of $\frac{\partial n(\mathbf{r})}{\partial u_{\mathbf{q}}}$. The A and B coefficients of Eqs. (A24) and (A25) are defined as

$$A^{(\alpha)}_{\substack{\mathbf{k},i\\ \mu,s}} = \frac{-i}{\Omega}\sum_{\mathbf{G}}\psi^*_{\mathbf{k},i}(\mathbf{G})e^{-i\mathbf{G}\cdot\mathbf{t}_s}(\mathbf{k}+\mathbf{G})_\alpha P_{\mu,s}(\mathbf{k}+\mathbf{G}), \quad A^{(\alpha,\beta)}_{\substack{\mathbf{k},i\\ \mu,s}} = \frac{(-i)^2}{\Omega}\sum_{\mathbf{G}}\psi^*_{\mathbf{k},i}(\mathbf{G})e^{-i\mathbf{G}\cdot\mathbf{t}_s}(\mathbf{k}+\mathbf{G})_\alpha(\mathbf{k}+\mathbf{G})_\beta P_{\mu,s}(\mathbf{k}+\mathbf{G}),$$
$$A^{(\alpha,\beta,\gamma)}_{\substack{\mathbf{k},i\\ \mu,s}} = \frac{(-i)^3}{\Omega}\sum_{\mathbf{G}}\psi^*_{\mathbf{k},i}(\mathbf{G})e^{-i\mathbf{G}\cdot\mathbf{t}_s}(\mathbf{k}+\mathbf{G})_\alpha(\mathbf{k}+\mathbf{G})_\beta(\mathbf{k}+\mathbf{G})_\gamma P_{\mu,s}(\mathbf{k}+\mathbf{G}).$$

$$B_{\substack{\mathbf{q},\mathbf{k},i\\ \mu,s}} = \frac{1}{\Omega}\sum_{\mathbf{G}}\left[\tilde{\phi}^{\mathbf{q}}_{\mathbf{k},i}(\mathbf{G})\right]^* P_{\mu,s}(\mathbf{k}+\mathbf{q}+\mathbf{G})e^{-i(\mathbf{q}+\mathbf{G})\cdot\mathbf{t}_s}, \quad B^{(\alpha)}_{\substack{\mathbf{q},\mathbf{k},i\\ \mu,s}} = \frac{-i}{\Omega}\sum_{\mathbf{G}}\left[\tilde{\phi}^{\mathbf{q}}_{\mathbf{k},i}(\mathbf{G})\right]^*(\mathbf{k}+\mathbf{q}+\mathbf{G})_\alpha P_{\mu,s}(\mathbf{k}+\mathbf{q}+\mathbf{G})e^{-i(\mathbf{q}+\mathbf{G})\cdot\mathbf{t}_s},$$
$$B^{(\alpha,\beta)}_{\substack{\mathbf{q},\mathbf{k},i\\ \mu,s}} = \frac{(-i)^2}{\Omega}\sum_{\mathbf{G}}\left[\tilde{\phi}^{\mathbf{q}}_{\mathbf{k},i}(\mathbf{G})\right]^*(\mathbf{k}+\mathbf{q}+\mathbf{G})_\alpha(\mathbf{k}+\mathbf{q}+\mathbf{G})_\beta P_{\mu,s}(\mathbf{k}+\mathbf{q}+\mathbf{G})e^{-i(\mathbf{q}+\mathbf{G})\cdot\mathbf{t}_s},$$

where the notation $(\mathbf{k}+\mathbf{G})_\alpha$ means the cartesian component α of vector $\mathbf{k}+\mathbf{G}$.

6. Nonlinear core correction

Within the pseudopotential approach, the electronic charge density is divided into core and valence contributions. A common way to include the core effects in the Kohn-Sham equations is the nonlinear core correction scheme of Ref. 36. In practice, one determines the charge density of the core electrons $n_{\mathrm{c}}(\mathbf{r})$ only once, before the KS self-consistent cycle, as $n_{\mathrm{c}}(\mathbf{r})$ only depends on the pseudopotentials. The KS equations are still solved only for the valence bands and $n(\mathbf{r})$ defined in Eq. (A3) remains the valence charge. On the contrary, in Eq. (A2), one substitutes $E_{\mathrm{I}}[n]$ with $E_{\mathrm{I}}[n_{\mathrm{t}}]$ where $n_{\mathrm{t}}(\mathbf{r}) = n(\mathbf{r}) + n_{\mathrm{c}}(\mathbf{r})$ is the total charge density.

By using this approach, the third-order equations need to be modified. First, in the last term in the right-hand side of Eq. (A12), one has to replace the three $\partial n/\partial u_{\mathbf{q}}$ with the corresponding $\partial n_{\mathrm{t}}/\partial u_{\mathbf{q}}$. Second, one has to include in the

right-hand side of Eq. (A12) the two additional terms

$$\int \frac{\delta E_{\rm I}[n_{\rm t}]}{\delta n(\mathbf{r})} \frac{\partial^3 n_{\rm c}(\mathbf{r})}{\partial u_{\mathbf{q}} \partial u_{\mathbf{q}'} \partial u_{\mathbf{q}''}} d\mathbf{r} + 3 \int \frac{\delta^2 E_{\rm I}[n_{\rm t}]}{\delta n(\mathbf{r}) \delta n(\mathbf{r}')} \frac{\partial^2 n_{\rm c}(\mathbf{r})}{\partial u_{\mathbf{q}} \partial u_{\mathbf{q}'}} \frac{\partial^2 n_{\rm t}(\mathbf{r}')}{\partial u_{\mathbf{q}''}} d\mathbf{r} d\mathbf{r}'. \quad \text{(A26)}$$

APPENDIX B: NOTES ON THE IMPLEMENTATION

This section discusses some practical issues concerning the actual implementation of the method.

1. Implementation

Let us consider three wave vectors in the general case in which $\mathbf{q} \neq \mathbf{q}' \neq \mathbf{q}''$, with $\mathbf{q} + \mathbf{q}' + \mathbf{q}'' = \mathbf{0}$. The calculations of the third-order derivatives is done in three consecutive steps. (1) Self-consistent calculation to obtain the ground-state charge $n(\mathbf{r})$ and the Kohn-Sham potential $V^{\rm KS}(\mathbf{r})$. (2) Self-consistent linear response calculation to determine $\partial n(\mathbf{r})/\partial u_{\tilde{\mathbf{q}}}$ and $\partial V^{\rm KS}(\mathbf{r})/\partial u_{\tilde{\mathbf{q}}}$. This is done three times for the three cases $\tilde{\mathbf{q}} = \mathbf{q}'$, $\mathbf{q}''$, and $\mathbf{q}''$. (3) Calculation of the third-order derivatives.

In order to do step 3, seven distinct sets of ground-state wave functions $|\psi\rangle$ are needed [see Eqs. (A13) or (A14)]: $|\psi_{\mathbf{k}}\rangle$, $|\psi_{\mathbf{k}+\tilde{\mathbf{q}}}\rangle$, $|\psi_{\mathbf{k}-\tilde{\mathbf{q}}}\rangle$, with $\tilde{\mathbf{q}} = \mathbf{q}$, $\mathbf{q}'$, and $\mathbf{q}''$, where $\mathbf{k}$ runs on the ensemble of wave vectors, which are used in the electronic integration. The $|\psi_{\mathbf{k}}\rangle$ are already calculated in step 1. They can be saved and read from disk or they can be calculated a second time with a relatively inexpensive non-self-consistent solution of the KS equation [based on the knowledge of $V^{\rm KS}$ and $n(\mathbf{r})$ determined in step 1]. When $\mathbf{k}$ runs on a regular grid and $\tilde{\mathbf{q}}$ belongs to the grid, the different sets might coincide. However, given the way the code is implemented[11] (the wave functions are read and written from sequential files; different processors might work with different $\mathbf{k}$ points in parallel), it is best to keep distinct the seven sets.

Twelve distinct sets of wave-function derivatives are also needed: $|\phi_{\mathbf{k}}^{\tilde{q}}\rangle$, $|\phi_{\mathbf{k}}^{-\tilde{q}}\rangle$, $|\phi_{\mathbf{k}-\tilde{\mathbf{q}}}^{\tilde{q}}\rangle$, and $|\phi_{\mathbf{k}+\tilde{\mathbf{q}}}^{-\tilde{q}}\rangle$, with $\tilde{\mathbf{q}} = \mathbf{q}$, $\mathbf{q}'$, and $\mathbf{q}''$. These wave functions can be calculated with a non-self-consistent solution of the linearized KS equation, which is based on the knowledge of the $\partial V^{\rm KS}(\mathbf{r})/\partial u_{\tilde{\mathbf{q}}}$ calculated in step 2. Even in this case, for practical reasons, it is better to keep distinct the twelve sets even when some of them coincide. These derivatives are computed resolving non-self-consistently Eq. (A1); in the present work, this was the most CPU intensive step; on the other hand, for bigger systems, the input/output of $\partial n/\partial u_{\mathbf{q}}$ can become a bottleneck.

In order to evaluate Eq. (A13), one needs to calculate matrix elements of the kind $\langle \phi_{\mathbf{k}}^{-\mathbf{q}} | V^{\mathbf{q}'} | \phi_{\mathbf{k}}^{\mathbf{q}''} \rangle$ and $\langle \psi_{\mathbf{k}-\mathbf{q}'} | V^{\mathbf{q}''} | \psi_{\mathbf{k}+\mathbf{q}} \rangle$. In both cases, this calculation has to be done six times for all the possible permutations of the three wave vectors $\mathbf{q}$, $\mathbf{q}'$, $\mathbf{q}''$. For the metallic case, Eq. (A14), further terms are needed. The terms $\langle \phi_{\mathbf{k}+\mathbf{q}_a}^{-\mathbf{q}_a} | V^{\mathbf{q}_b} | \psi_{\mathbf{k}+\mathbf{q}_b} \rangle$ need to be computed six times for $\mathbf{q}_a$ and $\mathbf{q}_b$ equal to $\mathbf{q}$, $\mathbf{q}'$, $\mathbf{q}''$, with $\mathbf{q}_a \neq \mathbf{q}_b$. The terms $\langle \psi_{\mathbf{k}+\mathbf{q}} | V^{\mathbf{q}} | \psi_{\mathbf{k}} \rangle$ and $\langle \psi_{\mathbf{k}-\mathbf{q}} | V^{-\mathbf{q}} | \psi_{\mathbf{k}} \rangle$ are computed already in step 2 and can be saved for later use in step 3. The terms $\langle \psi_{\mathbf{k}-\mathbf{q}} | V^{\mathbf{q}'} | \psi_{\mathbf{k}+\mathbf{q}''} \rangle$ need to be computed for the six permutations of $\mathbf{q}$, $\mathbf{q}'$, and $\mathbf{q}''$.

In some special cases, the number of operations can be greatly reduced. The most obvious one is when $\mathbf{q} = \mathbf{q}' = \mathbf{q}'' = \mathbf{0}$; in this case, only one set of wave function derivatives is needed: $|\phi_{\mathbf{k}}^{\mathbf{0}}\rangle$. Moreover, when $\mathbf{q} = \mathbf{0}$, $\mathbf{q}' = -\mathbf{q}'' = \mathbf{p}$, with $\mathbf{p} \neq \mathbf{0}$, only three sets of wave function derivatives are needed: $|\phi_{\mathbf{k}}^{\mathbf{0}}\rangle$, $|\phi_{\mathbf{k}}^{\mathbf{q}}\rangle$, and $|\phi_{\mathbf{k}-\mathbf{q}}^{\mathbf{q}}\rangle$. This is because $\partial n(\mathbf{r})/\partial u_{-\mathbf{q}} = [\partial n(\mathbf{r})/\partial u_{\mathbf{q}}]^*$ and, according to time reversal symmetry, $\phi_{-\mathbf{k}}^{-\mathbf{q}}(\mathbf{r}) = [\phi_{\mathbf{k}}^{\mathbf{q}}(\mathbf{r})]^*$. Another special case is when $\mathbf{q} = 2\mathbf{p}$, $\mathbf{q}' = \mathbf{q}'' = -\mathbf{p}$; in this case, eight derivatives are needed and the index permutation can be used to avoid computing some terms.

2. Symmetry and q points

A Bravais lattice can be invariant under a certain number, up to 48, of rotations. A crystal will respect a subset, possibly all, of these symmetries defining the group of crystal symmetries, $\mathcal{G}$. These symmetries can be exploited to reduce the computational cost of the calculation and must be enforced to avoid unphysical breaking of symmetry caused by computational noise. Here, we briefly revise how this is done in the PWSCF and PHONON codes of QUANTUM ESPRESSO, and we describe how the approach has been extended to the third order.

In the ground-state energy calculation, the Kohn-Sham equations [see Eqs. (A1)–(A3)] are not solved for all the $\mathbf{k}$ points of the chosen grid. Instead, they are solved only for a subset of $\mathbf{k}$ points, which are inequivalent under the rotations of $\mathcal{G}$ (these $\mathbf{k}$ points belong to the so called irreducible wedge of the BZ). The charge density $n(\mathbf{r})$ is then obtained, inexpensively, by summing on this $\mathbf{k}$-point subset and, then, by imposing the symmetries of the crystal. The symmetries are imposed by rotating the initial charge density according to all the symmetries and, then, by making the average. In general, even if the crystal has no symmetries, the sum can be performed on half of the $\mathbf{k}$ points of the initial grid since $\psi_{-\mathbf{k}}(\mathbf{r}) = \psi_{\mathbf{k}}^*(\mathbf{r})$ (time reversal symmetry).

In the phonon calculation, the situation depends on the phonon wave vector $\mathbf{q}$. Let us consider the symmetries of the crystal that are associated with a rotation that leaves $\mathbf{q}$ unchanged (or that transform $\mathbf{q}$ into an equivalent $\mathbf{q} + \mathbf{G}$). This subgroup of $\mathcal{G}$ is called the small group of $\mathbf{q}$, $\mathcal{G}_{\mathbf{q}}$. The linear response equations [see Eqs. (A7)–(A9)] are not solved on the grid. Instead, they are solved only for a subset of $\mathbf{k}$ points, which are inequivalent under the rotations of $\mathcal{G}_{\mathbf{q}}$. $\partial n(\mathbf{r})/\partial u_{\mathbf{q}}$ is obtained by summing on this $\mathbf{k}$-point subset and, then, by imposing the symmetries of $\mathcal{G}_{\mathbf{q}}$ [in analogy with $n(\mathbf{r})$ in the previous paragraph]. Because of time reversal symmetry, in order to obtain $\partial n(\mathbf{r})/\partial u_{\mathbf{q}}$ from Eq. (A9) one needs to compute explicitly only the $|\phi_{\mathbf{k}}^{\mathbf{q}}\rangle$ but not the $|\phi_{\mathbf{k}}^{-\mathbf{q}}\rangle$. However, if there are no other symmetries, the sum has to be performed on all the $\mathbf{k}$ points of the grid and not on half as in the total energy calculation. Once that $\partial n(\mathbf{r})/\partial u_{\mathbf{q}}$ has been calculated, one can determine the dynamical matrix at $\mathbf{q}$.

Another way in which the symmetries can be exploited is the following. The ensemble of the vectors obtained by rotating $\mathbf{q}$ with all the rotations of $\mathcal{G}$ is called the star of $\mathbf{q}$. The number

of inequivalent vectors in the star is $|\mathcal{G}|/|\mathcal{G}_{\mathbf{q}}|$, where $|\mathcal{G}|$ is the order of $\mathcal{G}$. Once that $\partial n(\mathbf{r})/\partial u_{\mathbf{q}}$ has been determined, all the $\partial n(\mathbf{r})/\partial u_{\tilde{\mathbf{q}}}$ for the vectors $\tilde{\mathbf{q}}$ in the star can be obtained inexpensively by rotation. Moreover, because of time reversal symmetry, $\partial n(\mathbf{r})/\partial u_{-\mathbf{q}} = [\partial n(\mathbf{r})/\partial u_{\mathbf{q}}]^*$.

A third-order calculation is conceptually not different. In this case, we are dealing with a triplet of points $(\mathbf{q},\mathbf{q}',\mathbf{q}'')$ and one has to consider the small group of the rotations of $\mathcal{G}$ that leave the three $\mathbf{q}$ points unchanged, $\mathcal{G}_{\mathbf{q},\mathbf{q}',\mathbf{q}''}$. The electronic $\mathbf{k}$-point summation in Eqs. (A13) and (A14) [and also those in Eqs. (A24) and (A25)] is done on a subset of points of the initial grid, which are inequivalent under the rotations of $\mathcal{G}_{\mathbf{q},\mathbf{q}',\mathbf{q}''}$. The third-order matrix obtained from this partial summation is not useful as it is. The actual third-order matrix is obtained by imposing on it the symmetries of $\mathcal{G}_{\mathbf{q},\mathbf{q}',\mathbf{q}''}$.

In analogy to the dynamical matrix case, once the third-order matrix of a given $(\mathbf{q},\mathbf{q}',\mathbf{q}'')$ triplet has been determined, on can apply the rotations $\mathcal{R}$ of the crystal symmetry group $\mathcal{G}$ and obtain inexpensively the matrices corresponding to the rotated triplet $(\mathcal{R}\mathbf{q},\mathcal{R}\mathbf{q}',\mathcal{R}\mathbf{q}'')$. Moreover, the matrix of the triplet $(-\mathbf{q},-\mathbf{q}',-\mathbf{q}'')$ can be obtained by conjugation. Another useful symmetry is the trivial one associated with the index permutation: by construction, the matrix associated with the triplet $(\mathbf{q},\mathbf{q}',\mathbf{q}'')$ is equal to the six matrices obtained by permuting the three vectors $\mathbf{q}$, $\mathbf{q}'$, $\mathbf{q}''$ and the corresponding indices.

3. Discretisation on a grid

In some cases, it is useful to calculate the third-order matrices on a regular grid of $\mathbf{q}$ wave vectors in the BZ, the reason for this is clarified in Appendix C. When we say that calculations are done on a given grid, it means that we have calculated the third-order coefficients corresponding to every triplet $(\mathbf{q},\mathbf{q}',\mathbf{q}'')$ of points, such that each vector belongs to the grid and that the condition $\mathbf{q}+\mathbf{q}'+\mathbf{q}''=G$ is satisfied.

In the actual implementation of the procedure, we first determine $\partial n(\mathbf{r})/\partial u_{\mathbf{q}}$ and the dynamical matrices on the grid of $\mathbf{q}$ wave vector. Exploiting the symmetries can allow an important reduction of the computational cost. Indeed, the actual *ab initio* calculation is done only for those $\mathbf{q}$ points that do not belong to the same star (defined in the previous section) or which are not equivalent to the opposite of a point already calculated. $\partial n(\mathbf{r})/\partial u_{\mathbf{q}}$ and the dynamical matrices for the other points are then obtained by rotation or conjugation. Once this is done, we perform the third-order calculations.

In practice, we can perform a double loop on the grid and chose $\mathbf{q}$ and $\mathbf{q}'$ so that they belong to the grid. The third vector is chosen as $\mathbf{q}''=-\mathbf{q}-\mathbf{q}'$. $\mathbf{q}''$ may not belong to the grid. $\mathbf{q}''$ is, however, still connected to a point in grid by a reciprocal lattice vector $\mathbf{G}$ and, thanks to Eq. (A16), we are not losing generality. Moreover,

$$\frac{\partial n(\mathbf{r})}{\partial u_{\mathbf{q}''}} = \frac{\partial n(\mathbf{r})}{\partial u_{\mathbf{q}''+\mathbf{G}}}$$

for every reciprocal space vector $\mathbf{G}$, and we can use the $\partial n(\mathbf{r})/\partial u_{\mathbf{q}}$ calculated on the original grid. Once a triplet has been computed, we can determine for free all the triplets that are equivalent by rotation, permutation of the indices, or by conjugation. Actually, some of these operations can be redundant, e.g., a certain rotation could be equivalent to a permutation, or to a conjugation. The triplets obtained in this way are deleted from the list of the "triplets to be done" and will not be computed in the following step of the loop. This procedure allows for a spectacular reduction in the number of triplets; in the graphene case, 4096 possible triplets are reduced to just 88 independent triplets.

APPENDIX C: FOURIER INTERPOLATION

Actual DFPT calculations are done on a relatively coarse grid of $\mathbf{q}$ wave vectors. Dynamical matrices and third-order coefficients are then obtained for a finer grid with a Fourier interpolation technique. In this section, first, we revise the Fourier interpolation technique as it is implemented in the standard QUANTUM ESPRESSO package. Then, we describe how the method has been generalized to the third-order force constants.

1. Second order

Let us consider a lattice with basis $\mathbf{a}_1,\mathbf{a}_2,\mathbf{a}_3$. The dynamical matrices $D_2\left(\begin{smallmatrix} s & \mathbf{q} \\ s' & \end{smallmatrix}\right)$ [we use the definition of Eq. (2) and we drop for simplicity the Cartesian indices] are first computed *ab initio* on a uniform grid, centered in the origin, of $N_1\times N_2\times N_3$ $\mathbf{q}$ points of the Brillouin zone. We want to determine the real space force constants

$$F_2\left(\begin{smallmatrix} s & \mathbf{R} \\ s' & \end{smallmatrix}\right) = \frac{\partial^2 \mathcal{E}^{\mathrm{tot}}}{\partial v_{\mathbf{0},s}\partial v_{\mathbf{R},s'}} \tag{C1}$$

by Fourier interpolation of the D_2 from the $N_1\times N_2\times N_3$ grid. D_2 for a generic $\mathbf{q}$ point can then be obtained by back Fourier interpolation.

Let us consider

$$\tilde{F}_2\left(\begin{smallmatrix} s & \mathbf{R} \\ s' & \end{smallmatrix}\right) = \frac{1}{N_{\mathrm{t}}}\sum_{\mathbf{q}} D_2\left(\begin{smallmatrix} s & \mathbf{q} \\ s' & \end{smallmatrix}\right) e^{-i\mathbf{q}\cdot\mathbf{R}}, \tag{C2}$$

where $\mathbf{R}$ is a lattice vector, $N_{\mathrm{t}}=N_1N_2N_3$, and the sum is performed on the points of the grid. The $\tilde{F}_2$ defined in this way cannot be used as they are since they are unphysical long-ranged constants. Indeed, $\tilde{F}_2\left(\begin{smallmatrix} s & \mathbf{R}+\overline{\mathbf{R}} \\ s' & \end{smallmatrix}\right) = \tilde{F}_2\left(\begin{smallmatrix} s & \mathbf{R} \\ s' & \end{smallmatrix}\right)$ for any $\overline{\mathbf{R}}$ vector of the superlattice (SL) generated by the lattice vectors $\mathbf{A}_1=N_1\mathbf{a}_1$, $\mathbf{A}_2=N_2\mathbf{a}_2$, $\mathbf{A}_3=N_3\mathbf{a}_2$.

The short-ranged F_2 can be obtained from the $\tilde{F}_2$ in the following way. We define two vectors as "SL equivalent" when their difference is a vector of the superlattice defined by $\mathbf{A}_1$, $\mathbf{A}_2$, $\mathbf{A}_3$ and we call W_{SL} as the Wigner-Seitz of this superlattice. Equation (C1) is the force constant between the atoms whose distance is $\mathbf{d}=\mathbf{R}+\mathbf{t}_{s'}-\mathbf{t}_s$, where $\mathbf{t}_s$ is the position of the atom s in the unit cell. We distinguish three cases: (i) when $\mathbf{d}\in W_{\mathrm{SL}}$, $F_2\left(\begin{smallmatrix} s & \mathbf{R} \\ s' & \end{smallmatrix}\right) = \tilde{F}_2\left(\begin{smallmatrix} s & \mathbf{R} \\ s' & \end{smallmatrix}\right)$, (ii) when $\mathbf{d}$ lies on the border of W_{SL}, $F_2\left(\begin{smallmatrix} s & \mathbf{R} \\ s' & \end{smallmatrix}\right) = \tilde{F}_2\left(\begin{smallmatrix} s & \mathbf{R} \\ s' & \end{smallmatrix}\right)/N_{\mathrm{eq}}$, where N_{eq} is the number of points on the border of W_{SL} which are "SL equivalent" to $\mathbf{d}$, and (iii) when $\mathbf{d}\notin W_{\mathrm{SL}}$, $F_2\left(\begin{smallmatrix} s & \mathbf{R} \\ s' & \end{smallmatrix}\right)=0$. The interpolated dynamical

matrix for a generic $\mathbf{q}$ is then

$$D_2\begin{pmatrix} s & \mathbf{q} \\ s' & \end{pmatrix} = \sum_{\mathbf{R}} F_2\begin{pmatrix} s & \mathbf{R} \\ s' & \end{pmatrix} e^{i\mathbf{q}\cdot\mathbf{R}}, \tag{C3}$$

where the sum is done on all the lattice vectors $\mathbf{R}$. This is the Fourier interpolation technique as it is implemented in the standard QUANTUM ESPRESSO package.

2. Third order

For the third-order coefficients the situation is analogous, although less straightforward. We use the following notations:

$$\begin{aligned} D_3\begin{pmatrix} s & \mathbf{q} & \mathbf{q}' & \mathbf{q}'' \\ & s' & s'' & \end{pmatrix} &= \frac{1}{N}\frac{\partial^3 \mathcal{E}^{\text{tot}}}{\partial u_{\mathbf{q},s}\partial u_{\mathbf{q}',s'}\partial u_{\mathbf{q}'',s''}}, \\ F_3\begin{pmatrix} s & \mathbf{R} & \mathbf{R}' & \mathbf{R}'' \\ & s' & s'' & \end{pmatrix} &= \frac{\partial^3 \mathcal{E}^{\text{tot}}}{\partial v_{\mathbf{R},s}\partial v_{\mathbf{R}',s'}\partial v_{\mathbf{R}'',s''}}. \end{aligned} \tag{C4}$$

The matrices D_3 are first computed *ab initio* on a uniform grid of $\mathbf{q}$ points centered in the origin, meaning that both vectors $\mathbf{q}'$ and $\mathbf{q}''$ run on the grid, while $\mathbf{q} = -\mathbf{q}' - \mathbf{q}''$. We then define

$$\begin{aligned} &\tilde{F}_3\begin{pmatrix} \mathbf{0} & \mathbf{R}' & \mathbf{R}'' \\ s & s' & s'' \end{pmatrix} \\ &= \frac{1}{N_{\text{t}}^2}\sum_{\mathbf{q}',\mathbf{q}''} D_3\begin{pmatrix} \mathbf{q} & \mathbf{q}' & \mathbf{q}'' \\ s & s' & s'' \end{pmatrix} e^{-i(\mathbf{q}'\cdot\mathbf{R}'+\mathbf{q}''\cdot\mathbf{R}'')}, \end{aligned} \tag{C5}$$

where the sums are performed on the grid points.

The force constants F_3 of Eq. (C4) correspond to three atoms at the positions $\mathbf{t}_s$, $\mathbf{t}_{s'} + \mathbf{R}'$, and $\mathbf{t}_{s''} + \mathbf{R}''$ (because of the crystal translational symmetry we can consider without loss of generality $\mathbf{R} = \mathbf{0}$). The three atoms form a triangle with perimeter $P = |\mathbf{d}_1| + |\mathbf{d}_2| + |\mathbf{d}_3|$, where $\mathbf{d}_1$, $\mathbf{d}_2$, $\mathbf{d}_3$ are the distances among the three atoms (the three sides of the triangle). To determine F_3, we consider three cases. (i) When all the three distances $\mathbf{d}_1$,$\mathbf{d}_2$,$\mathbf{d}_3$ are inside (and not on the border) of W_{SL}, we put $F_3(\begin{smallmatrix} \mathbf{0} & \mathbf{R}' & \mathbf{R}'' \\ s & s' & s'' \end{smallmatrix}) = \tilde{F}_3(\begin{smallmatrix} \mathbf{0} & \mathbf{R}' & \mathbf{R}'' \\ s & s' & s'' \end{smallmatrix})$. (ii) If two of the distances (e.g., $\mathbf{d}_1$,$\mathbf{d}_2$) are inside W_{SL} and the third one is outside or on the border of W_{SL}, we calculate the perimeter P of the triangle. If P is the shortest perimeter among the perimeters of all the triangles formed by the triplet of atoms "SL equivalent" to the original three, we put $F_3(\begin{smallmatrix} \mathbf{0} & \mathbf{R}' & \mathbf{R}'' \\ s & s' & s'' \end{smallmatrix}) = \tilde{F}_3(\begin{smallmatrix} \mathbf{0} & \mathbf{R}' & \mathbf{R}'' \\ s & s' & s'' \end{smallmatrix})/N_{\text{eq}}$, where N_{eq} is the number of triangles with perimeter equal to P. (iii) In all the other cases $F_3(\begin{smallmatrix} \mathbf{0} & \mathbf{R}' & \mathbf{R}'' \\ s & s' & s'' \end{smallmatrix}) = 0$.

The interpolated D_3 matrices for a generic triplet of wave vectors (such that $\mathbf{q} + \mathbf{q}' + \mathbf{q}'' = \mathbf{G}$) are obtained from

$$D_3\begin{pmatrix} s & \mathbf{q} & \mathbf{q}' & \mathbf{q}'' \\ & s' & s'' & \end{pmatrix} = \sum_{\mathbf{R}',\mathbf{R}''} F_3\begin{pmatrix} s & \mathbf{0} & \mathbf{R}' & \mathbf{R}'' \\ & s' & s'' & \end{pmatrix} e^{i(\mathbf{q}'\cdot\mathbf{R}'+\mathbf{q}''\cdot\mathbf{R}'')}, \tag{C6}$$

where the sums run on all the lattice vectors. The criterion presently described to determine the F_3s stems from the assumption of a long-range exponential decay of the force constants.

APPENDIX D: COMPUTATIONAL DETAILS

1. Electronic integration

The electronic integration of the density functional theory calculations is done using the first-order Methfessel-Paxton smearing[32] of 0.02 Ry, which converges for a grid of $32 \times 32 \times 1$ electronic $\mathbf{k}$ points in simple and bilayer graphene and for a grid of $32 \times 32 \times 8$ $\mathbf{k}$ points for graphite.

2. Linear response calculations

DFT dynamical matrices are corrected using a procedure based on DFT + GW renormalization of the electron-phonon interaction as in Ref. 24. Indeed, DFT reproduces very well the measured dispersions of graphite for all the phonon branches but for the TO one, in the vicinity of the high-symmetry point $\mathbf{K}$. This failure of DFT, which is very specific to the graphene and graphite systems, has been analyzed in Ref. 24. To improve the accuracy of the TO phonon branch, we have applied an electron-phonon self-interaction as described in Ref. 24. The detailed procedure is described in Sec. II B of Ref. 37 (third paragraph). We have used the parameter $r^{GW} = 1.65$, which is appropriate to the present LDA calculations and which can be derived from Table I of Ref. 24. Using this approach, we determined the dynamical matrices of graphene on a supersampled $48 \times 48 \times 1$ $\mathbf{q}$-point grid. The matrices for the graphite and for the bilayer are then obtained by using as in-plane force constants those of graphene and as out-of-plane force constants those coming from independent DFPT calculations on the two systems.

The third-order coefficients are obtained in the standard way, that is, without including this self-interaction correction of Ref. 24. For graphene, the third-order coefficients are calculated on a $8 \times 8 \times 1$ $\mathbf{q}$-point grid (see Appendix B 3), which consists in 88 irreducible triplets. For bulk graphite, the third-order coefficients are calculated on a $8 \times 8 \times 2$ grid, which consists in 297 irreducible $\mathbf{q}$ triplets. When computing the linewidth, we have tested convergence starting from the $8 \times 8 \times 2$ grid coefficients, finding that the use of the those from the $4 \times 4 \times 2$ subset grid (33 inequivalent triplets) does not worsen accuracy. For bilayer graphene, the third-order coefficients are calculated on a $4 \times 4 \times 1$ $\mathbf{q}$-point grid (12 irreducible triplets).

3. Broadening calculations

Equations (6) and (7) are evaluated by performing the sum over a discrete uniform grid of $\mathbf{q}$ points randomly shifted from the origin. The $\delta(x)$ distribution is substituted with the Gaussian function $\tilde{\delta}(x) = e^{-(x/\chi)^2}/(\chi\sqrt{\pi})$, where χ is an artificial smearing, independent from $\mathbf{q}$. The results of Secs. III A and III B are obtained by using for graphene, a $1800 \times 1800 \times 1$ grid and $\chi = 1$ cm^{-1}, for graphite, a $600 \times 600 \times 15$ grid and $\chi = 5$ cm^{-1}, and for the bilayer, a $1200 \times 1200 \times 1$ grid and $\chi = 2$ cm^{-1}. The results of Sec. III C are obtained using for graphene, a $128 \times 128 \times 1$ grid and $\chi = 10$ cm^{-1} and for graphite and bilayer, a $64 \times 64 \times 4$ grid and $\chi = 10$ cm^{-1}. For each system, the same grid is used to determine the broadening from Eq. (6) and the thermal conductivity from Eq. (7). The convergence has been tested using smaller smearing values and finer grids at selected temperatures.

*lorenzo.paulatto@impmc.upmc.fr

[1] G. D. Mahan, B. Sales, and J. Sharp, Phys. Today **50**, 42 (1997); F. J. Di Salvo, Science **285**, 703 (1999).

[2] D. G. Cahill, W. K. Ford, K. E. Goodson, G. D. Mahan, A. Majumdar, H. J. Maris, R. Merlin, and S. R. Phillpot, J. Appl. Phys. **93**, 793 (2003).

[3] S. Narasimhan and D. Vanderbilt, Phys. Rev. B **43**, 4541 (1991).

[4] X. Tang, C. W. Li, and B. Fultz, Phys. Rev. B **82**, 184301 (2010); X. Tang and B. Fultz, *ibid*. **84**, 054303 (2011).

[5] D. Donadio and G. Galli, Phys. Rev. Lett. **99**, 255502 (2007).

[6] D. A. Broido, M. Malorny, G. Birner, N. Mingo, and D. Stewart, Appl. Phys. Lett. **91**, 231922 (2007).

[7] A. Ward, D. A. Broido, D. A. Stewart, and G. Deinzer, Phys. Rev. B **80**, 125203 (2009); A. Ward and D. A. Broido, *ibid*. **81**, 085205 (2010).

[8] J. Garg, N. Bonini, B. Kozinsky, and N. Marzari, Phys. Rev. Lett. **106**, 045901 (2011).

[9] N. Bonini, J. Grag, and N. Marzari, Nano Lett. **12**, 2673 (2012).

[10] S. Baroni, S. de Gironcoli, A. Dal Corso, and P. Giannozzi, Rev. Mod. Phys. **73**, 515 (2001).

[11] QUANTUM ESPRESSO is an open source distribution available at http://www.quantum-espresso.org; P. Giannozzi, S. Baroni, N. Bonini, M. Calandra, R. Car, C. Cavazzoni, D. Ceresoli, G. L. Chiarotti, M. Cococcioni, I. Dabo, A. D. Corso, S. de Gironcoli, S. Fabris, G. Fratesi, R. Gebauer, U. Gerstmann, C. Gougoussis, A. Kokalj, M. Lazzeri, L. Martin-Samos, N. Marzari, F. Mauri, R. Mazzarello, S. Paolini, A. Pasquarello, L. Paulatto, C. Sbraccia, S. Scandolo, G. Sclauzero, A. P. Seitsonen, A. Smogunov, P. Umari, and R. M. Wentzcovitch, J. Phys.: Condens. Matter **21**, 395502 (2009).

[12] X. Gonze and J.-P. Vigneron, Phys. Rev. B **39**, 13120 (1989).

[13] A. Debernardi, S. Baroni, and E. Molinari, Phys. Rev. Lett. **75**, 1819 (1995); A. Debernardi and S. Baroni, Solid State Commun. **91**, 813 (1994).

[14] M. Lazzeri and S. de Gironcoli, Phys. Rev. B **65**, 245402 (2002).

[15] M. Lazzeri, M. Calandra, and F. Mauri, Phys. Rev. B **68**, 220509 (2003).

[16] G. Deinzer, G. Birner, and D. Strauch, Phys. Rev. B **67**, 144304 (2003).

[17] G. P. Srivastava, Pramana **3** (1974); M. Asen-Palmer, K. Bartkowski, E. Gmelin, M. Cardona, A. P. Zhernov, A. V. Inyushkin, A. Taldenkov, V. I. Ozhogin, K. M. Itoh, and E. E. Haller, Phys. Rev. B **56**, 9431 (1997); J. X. Cao, X. H. Yan, Y. Xiao, and J. W. Ding, *ibid*. **69**, 073407 (2004); A. Khitun and L. Wang, Appl. Phys. Lett. **79**, 851 (2001).

[18] A. A. Balandin, Nat. Mater. **10**, 569 (2011).

[19] J. H. Seol, I. Jo, A. L. Moore, L. Lindsay, Z. H. Aitken, M. T. Pettes, X. Li, Z. Yao, R. Huang, D. Broido, N. Mingo, R. S. Ruoff, and L. Shi, Science **328**, 213 (2010).

[20] J. M. Ziman, *Electrons and Phonons: The Theory of Transport Phenomena in Solids* (Oxford University Press, USA, 2001).

[21] J. Maultzsch, S. Reich, C. Thomsen, H. Requardt, and P. Ordejón, Phys. Rev. Lett. **92**, 075501 (2004).

[22] M. Mohr, J. Maultzsch, E. Dobardžić, S. Reich, I. Milošević, M. Damnjanović, A. Bosak, M. Krisch, and C. Thomsen, Phys. Rev. B **76**, 035439 (2007).

[23] S. Piscanec, M. Lazzeri, F. Mauri, A. C. Ferrari, and J. Robertson, Phys. Rev. Lett. **93**, 185503 (2004).

[24] M. Lazzeri, C. Attaccalite, L. Wirtz, and F. Mauri, Phys. Rev. B **78**, 081406 (2008).

[25] N. Mounet and N. Marzari, Phys. Rev. B **71**, 205214 (2005).

[26] N. Bonini, M. Lazzeri, N. Marzari, and F. Mauri, Phys. Rev. Lett. **99**, 176802 (2007).

[27] L. Lindsay, D. A. Broido, and N. Mingo, Phys. Rev. B **82**, 115427 (2010).

[28] M. Balkanski, R. F. Wallis, and E. Haro, Phys. Rev. B **28**, 1928 (1983).

[29] C. Y. Ho, R. W. Powell, and P. E. Liley, *Thermal Conductivity of the Elements: A Comprehensive Review: Journal of Physical and Chemical Reference Data* (American Chemical Society, Washington, DC, 1974), pp. I–164.

[30] L. Lindsay, D. A. Broido, and N. Mingo, Phys. Rev. B **83**, 235428 (2011).

[31] R. M. Martin, *Electronic Structure* (Cambridge University Press, Cambridge, 2004).

[32] M. Methfessel and A. T. Paxton, Phys. Rev. B **40**, 3616 (1989).

[33] S. de Gironcoli, Phys. Rev. B **51**, 6773 (1995).

[34] P. P. Ewald, Ann. Phys. **369**, 253 (1921).

[35] L. Kleinman and D. M. Bylander, Phys. Rev. Lett. **48**, 1425 (1982).

[36] S. G. Louie, S. Froyen, and M. L. Cohen, Phys. Rev. B **26**, 1738 (1982).

[37] P. Venezuela, M. Lazzeri, and F. Mauri, Phys. Rev. B **84**, 035433 (2011).